

Geothermal potential in Singapore explored with non-invasive seismic data



Yiming Bai^a, Shijie Hao^a, Jinyun Xie^{a,b,1}, Mijian Xu^{a,1}, Xiao Xiao^a, Jing Chen^a, Chun Fei Chey^a, Dongdong Wang^a, Ping Tong^{a,c,*}

^a Division of Mathematical Sciences, School of Physical and Mathematical Sciences, Nanyang Technological University, Singapore

^b Hubei Subsurface Multi-scale Imaging Key Laboratory, School of Geophysics and Geomatics, China University of Geosciences, Wuhan, China

^c Earth Observatory of Singapore, Nanyang Technological University, Singapore

ARTICLE INFO

Keywords:
Geothermal exploration
Hot spring
Upper crustal structure
Seismic imaging
Tomography
Singapore

ABSTRACT

Singapore is dedicated to developing geothermal resources to meet rising energy demand and achieve net-zero emissions by 2050. While above-average heat flow and local hot springs suggest high geothermal potential beneath Singapore, the associated deep thermal sources remain underexplored due to a limited understanding of the subsurface structure. Applying ambient noise tomography and converted/reflected body-wave imaging to new seismic data from North Singapore reveals a highly fractured, fluid-saturated shallow geothermal reservoir located southeast of the Sembawang Hot Spring in the Yishun district. This reservoir exhibits low V_s ($< 3.2 \text{ km/s}$) and high V_p/V_s (> 2.1). At a greater depth of $\sim 4 \text{ km}$, a crustal seismic discontinuity indicates a transition from the upper Bukit Timah Granite to the porous metasedimentary basement, where a deep aquifer might form, supplying the shallow reservoir and, ultimately, the Sembawang Hot Spring through the fault and fracture system. Our results highlight Yishun as a potential site for deep drilling in future geothermal explorations, and more broadly, provide new insights into the deep heat sources of numerous medium-to-low enthalpy geothermal sites throughout the Southeast Asian batholiths.

1. Introduction

1.1. Motivations

As a densely populated yet resource-scarce city state, Singapore is committed to achieving net-zero emissions by 2050 and diversifying its energy portfolio. Geothermal energy plays a crucial role in these efforts due to its minimal greenhouse gas release and its capacity for natural replenishment, unaffected by weather conditions or commodity price fluctuations (Barbier, 2002; Stober and Bucher, 2021). Singapore potentially possesses a wealthy amount of deep geothermal power. This is evidenced by a high regional heat flow of $110\text{--}130 \text{ mW/m}^2$ (Hall and Morley, 2004; Oliver et al., 2011), which is twice the continental average (Stober and Bucher, 2021), and by the discovery of local thermal springs, notably at Sembawang in North Singapore and another group on the eastern offshore island (Fig. 1). The Sembawang hot spring (SHS) has been the center for exploring the geothermal potential in Singapore. There, surface spring water temperatures are measured at $60\text{--}70^\circ\text{C}$. A recent deep drilling north of the SHS reports prospective

temperature of $\sim 90^\circ\text{C}$ at 1.1 km depth (Tan, 2024). 2-D geothermal reservoir simulations further predict that groundwater temperatures at 4 km and deeper below the SHS may reach 200°C , viable for power generation (Stober and Bucher, 2021; Tjiawi, 2013). Generally, hot springs in tectonically stable regions are fed by radioactive heat generated within intrusive and/or sedimentary rocks, with faults serving as conduits for heat transfer (Alfarro and Wallace, 1994). Applying to Singapore, Zhao et al. (2002) propose that the SHS is part of a hydrothermal circulation system, where high-altitude meteoric water infiltrates the ground, heats up by contact with hot rock masses, and then rises to the spring orifices through faults or fractures. This is supported by local shallow boreholes, which have encountered fractured granitic rocks and water-bearing faults at $\sim 20\text{--}100 \text{ m}$ depths (Zhao et al., 2002). Similar conceptual models have been frequently adopted to explain the mechanisms of other low-temperature geothermal fields globally (e.g., Amatyakul et al., 2023; Axelsson et al., 2010; Liberty, 1998). Although earlier studies suggest promising geothermal potential at the SHS in North Singapore, existing geophysical investigations using well-logging are confined to shallow depths up to $50\text{--}200 \text{ m}$ or at one costly deep-

* Corresponding author at: Division of Mathematical Sciences, School of Physical and Mathematical Sciences, Nanyang Technological University, Singapore.
E-mail address: tongping@ntu.edu.sg (P. Tong).

¹ Now at Department of Earth Sciences, University of Toronto, ON, Canada.

penetration site. Therefore, their results provide inadequate spatial resolution of subsurface conditions at depths of $\sim 1\text{--}5$ km, where geothermal heat sources are commonly positioned (Domra Kana et al., 2015; Stober and Bucher, 2021). Delineating the detailed distribution of these sources, a prerequisite for commercial geothermal production, requires further 3-D mapping, ideally through approaches with minimal environmental impact. In response to this urgent need, a 16 million SGD investment has been allocated by the Singapore government for a two-year, non-invasive geophysical investigation to assess shallow-crustal geothermal resources nationwide, starting in mid-2024 (Tan, 2024). Our study, conducted independently and in parallel with the governmental initiatives, represents one of the first geophysical investigations into Singapore's deep geothermal resources.

While the aforementioned logging method can directly examine the effects of deep geothermal activities, its high cost restricts its application to carefully chosen sites, which often relies on detailed subsurface characterization, realized commonly by indirect methods (Domra Kana et al., 2015). For instance, geoelectrical imaging that measures subsurface electrical resistivity is effective in geothermal detection for its ability to detect fractured rocks and geothermal fluids (Muñoz, 2014). Within this category, magnetotellurics, known for its deep investigation capabilities, may not be feasible for Singapore, as the recorded natural signals are easily polluted by electromagnetic noise prevalent in urban areas; controlled-source electromagnetics, on the other hand, is better suitable for targeting shallow, engineering-scale geothermal prospects (Védrine et al., 2023). Furthermore, active seismic surveys that are widely used in the petroleum industry could pose complicated logistical issues when operating invasive sources in densely populated

metropolises. As a result, only short transects for mapping the upper few-hundred-meter structure have been conducted in Singapore (Pan et al., 2018). Alternatively, passive seismic methods using natural earthquakes and ambient noise have increasingly been applied for geothermal reservoir imaging at high-enthalpy volcanic sites, where geothermal systems exhibit distinct physical contrasts to surrounding rocks (e.g., Granados-Chavarría et al., 2022; Julian et al., 1996; Muksin et al., 2013; Planès et al., 2020). However, due to concerns like lower profitability, their applications are less common in medium-to-low enthalpy zones, as demonstrated in Singapore. Further, traditional routines often rely on a network of bulky seismometers, which requires significant space and relatively quiet environments – conditions not easily met in Singapore. Recent cost- and time-efficient node instrumentation boosts the use of passive seismic sources in urban settings (e.g., Cheng et al., 2021; Lin et al., 2013; Liu et al., 2025; Lythgoe et al., 2020). An earlier nationwide nodal experiment in Singapore successfully determined the first-order crustal structure (Lythgoe et al., 2020; Nilot et al., 2020). However, comprehensive 3-D crustal imaging at the scale needed for geothermal assessment in Singapore remains lacking.

Leveraging a nodal array newly deployed around the SHS, we assess the geothermal potential of Singapore through examining its seismic structure from surface to ~ 10 km depth. A 3-D isotropic V_s model in the upper 3 km of the crust is built using the adjoint-state ambient noise tomography method (Hao et al., 2024; Tong, 2021). Additionally, the V_p/V_s ratio, an important parameter that complements V_s for subsurface characterization, is confined by high-frequency earthquake-generated body waves; these waves are also used to identify intra-crustal seismic discontinuities. The resulting shallow-crustal images provide new

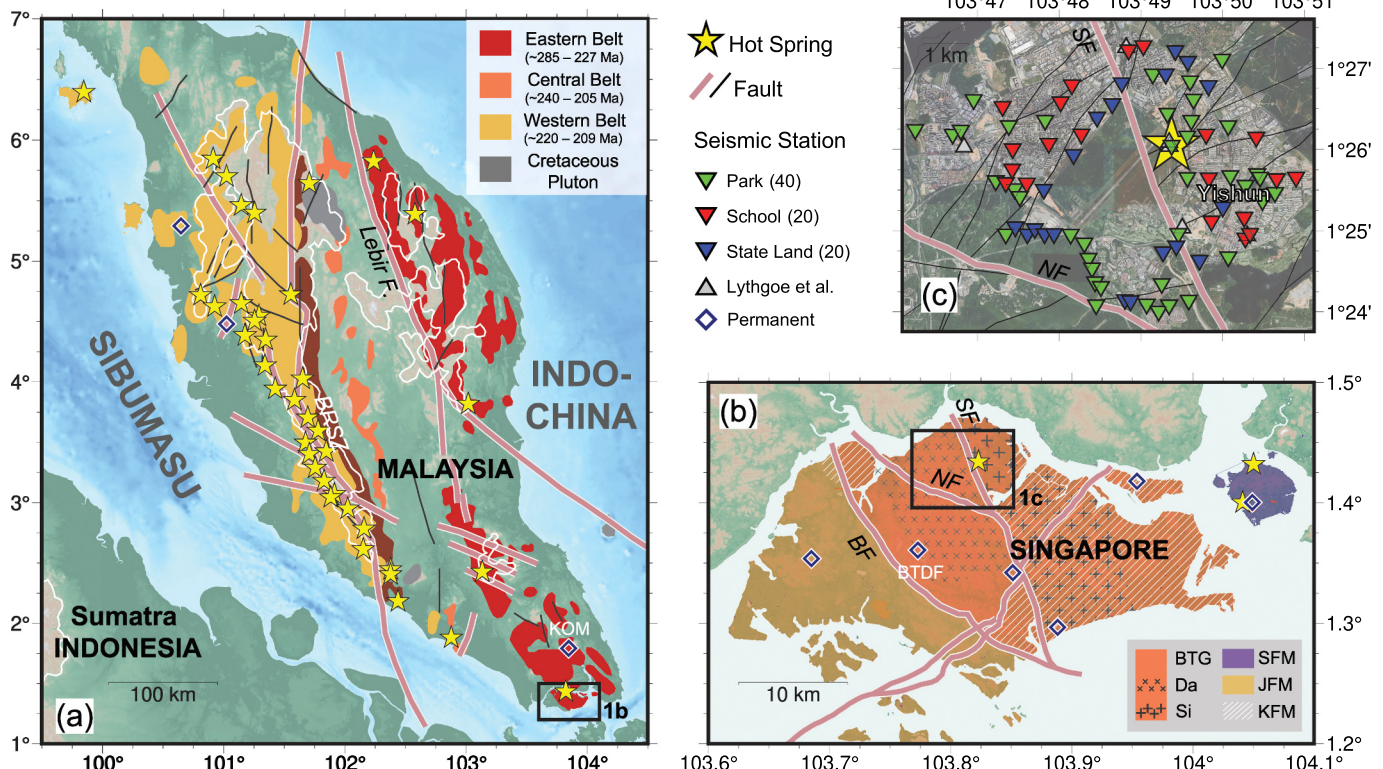


Fig. 1. Overview of the study area. (a) Geological setting of Peninsular Malaya and surroundings, showing distributions of granitoid provinces (with ages indicated in the legend), hot springs, faults and topography (Baioumy et al., 2015; Gillespie et al., 2019). White lines outline high-altitude regions of >300 m. Diamonds denote the Malaysian National Seismic Network. The black box outlines the area shown in (b). BRSZ – Bentong-Raub Suture Zone. (b) Map showing the major geological units of Singapore, hot springs, major faults (Leslie et al., 2019) and the Singapore Seismological Network. The black box outlines the study area. BTG – Bukit Timah Granite; Da – Dairy Farm Pluton; Si – Simpang Pluton; SFM – Sajahat Formation; JFM – Jurong Formation; KFM – Kallang Formation; BF – Bukit Timah Fault; NF – Nee Soon Fault; SF – Seletar Fault (c) Map showing the station distribution of the Sembawang array (40 in parks, 20 in schools and 20 on the state land) and of a previous nation-wide study (Lythgoe et al., 2020). The station, the SHS (star) and faults are superimposed on the aerial photograph of the area. The Yishun District mentioned in the text is highlighted.

insights into the geothermal process at Sembawang and serve as vital references for future geophysical investigations (e.g., when selecting optimal deep drilling sites) in Singapore, thereby supporting the nation's relentless energy development efforts.

1.2. Geological background

Singapore shares the same geological framework with Peninsular Malaya as part of Southeast Asia. Located ~500 km from the active India-Australia subduction front, this region exhibits geological imprints that are mostly remnants of ancient Tethyan plate subduction. The ~N-S trending Bentong-Raub Suture Zone in Peninsular Malaya marks the late Triassic collision boundary between two continental fragments – Sibumasu to the west and Indochina to the east, both of which separated from Gondwana at different times during the Paleozoic era (Fig. 1a) (Metcalfe, 2013). Field investigations distinguish three sub-parallel granitoid belts that form the southern component of sinuous batholiths extending throughout Southeast Asia (including Singapore, Malaysia, Thailand and Myanmar) (Hutchison and Tan, 2009; Metcalfe, 2013). These belts exhibit a westward younging trend, likely resulting from progressive rollback of the Tethyan slab and potential polarity-reversed underthrusting (Metcalfe, 2000; Ng et al., 2015; Oliver et al., 2014). The Western Belt comprises I- and S-type granitoids of Upper Triassic to Cenozoic ages and hosts 80 % of more than 60 hot springs found in West Malaysia, with surface temperatures ranging in 41–99 °C (Baioumy et al., 2015). To the east, across the Bentong-Raub Suture Zone, the Central and Eastern Belts are dominated by calc-alkaline, metaluminous, I-type granitoid from the Early Permian to Upper Triassic periods; the two belts are separated by the transcurrent Lebir Fault (Hutchison and Tan, 2009). Additionally, scattered I-type plutons of Cretaceous age, which are unrelated to earlier intrusions, are found in both belts.

Singapore lies at the southern tip of Peninsular Malaya and comprises three major geological units (Fig. 1b). The majority of West Singapore is underlain by the Middle Triassic, mildly metamorphosed volcanosediments of the Jurong Formation (Dodd et al., 2019). Moving eastward across the prominent Bukit Timah Fault Zone, the remaining two-thirds of onshore Singapore is dominated by the plutonic rocks of the Bukit Timah Granite (BTG), with much of its eastern area covered by the younger Quaternary shallow marine and terrestrial Kallang Formation (Leslie et al., 2019; Zhao, 1998). Zircon dating confirms the affinity of the Singapore intrusions with those of the Malaysian Eastern Belt, suggesting that the BTG dates from the Late Permian to Upper Triassic (Ng et al., 2015; Oliver et al., 2011, 2014). More recent studies indicate that the BTG consists of at least five discrete plutons, emplaced sequentially over a period of ~55 Ma (Gillespie et al., 2019). Among them the youngest Simpang pluton, located east of the Seletar Fault, hosts the SHS. While the geochronology and geochemistry of the BTG are relatively well documented, its physical properties, such as elastic velocity and thickness, remain underexplored. Acquiring detailed knowledge of the structures of these plutonic rocks would significantly enhance our understanding of the origin of the SHS, and by analogy, the other granite-hosted hot springs across Southeast Asia.

2. Data and methods

2.1. Seismic data

From 11 May to 30 September 2023, 80 three-component 5-Hz SmartSolo or ZLand nodes were deployed in the study area located around the SHS in North Singapore, with a station spacing of ~100–500 m (Fig. 1c). All the stations recorded continuous data for more than 50 days, with half exceeding 100 days. Our seismic data and methods allow fine-resolution imaging down to ~5 km depth, despite no stations being placed in the restricted zones immediately west of the hot spring. This depth range extends beyond that of existing boreholes (Gillespie et al.,

2019) and was only coarsely resolved by previous large-scale seismic studies (Lythgoe et al., 2020; Macpherson et al., 2013; Nilot et al., 2020). We carry out time-frequency and beamforming analyses on the nodal data and identify relatively high noise levels (Fig. S1) and complex noise distribution in North Singapore (Fig. S2). To extract reliable information from the nodal data, we apply stacking for noise suppression, with a consequence of slightly reduced spatial resolution. While we mainly focus on data collected from the Sembawang array, we also incorporate teleseismic data recorded by open-access stations outside of the study area for a more comprehensive discussion.

2.2. Ambient noise cross-correlation and tomography

Rayleigh-wave dispersion derived from ambient noise interferometry is well suited for imaging local-scale, shallow V_s structures potentially associated with geothermal activities. This technique is particularly valuable for Singapore, which is located in a seismically quiet region. We process continuous ambient noise data following the procedures documented by Bensen et al. (2007). The vertical-component seismic waveforms at each station are cut into hour-length segments with a 20-min overlap. After removing mean, trend and instrument response, the data are down-sampled from 250 Hz to 50 Hz and bandpass filtered between 50 s and 20 Hz. Biases, such as those caused by instrumental irregularities and earthquake signals, are suppressed by running mean normalization and spectral whitening. Subsequently, hourly cross-correlations are computed then linearly stacked for each station pair, followed by manual extraction of fundamental-mode Rayleigh-wave phase velocities, using an image transformation method (Yao et al., 2006). We exclude measurements with an inter-station distance less than one wavelength of Rayleigh waves (Luo et al., 2015) and those of low signal-to-noise ratio. We also discard asymmetric cross-correlations, which likely result from unevenly distributed urban noise (Figs. S1–S2). Eventually, we obtain dispersion data in the period band of 0.2–2.3 s; those at periods shorter than 2 s with more than 100 measurements (Fig. 2d) are used for tomography. Our dispersion measurements are sensitive to the V_s structure down to ~3 km (Fig. 3b).

The inter-station phase velocity dispersion data are inverted directly for the 3-D shear velocity structure in the upper 3 km depth beneath Sembawang and its vicinity, using the newly developed adjoint-state surface-wave tomography (Hao et al., 2024). We first fit the average of all the observed dispersion curves through a 1-D inversion, which provides a horizontally homogeneous V_s model. This model is employed as the initial model for the 3-D tomographic inversion. The computational domain is a volume of ~8 × 6 × 3 km³. To ensure high numerical accuracy, we use a dense forward grid with horizontal dimensions of 0.15 km and vertical dimensions of 0.2 km. The inversion grid, where the V_s perturbations are interpolated, comprises five sets of coarse regular grids, with grid sizes determined by checkerboard resolution tests (Fig. S3). A step-size-controlled gradient descent method is applied to iteratively update the model parameters (Tong, 2021). The final 3-D V_s model is obtained after 30 iterations. Throughout the inversion, the data misfit is reduced by 54.7 %, and the root mean square of the Rayleigh-wave traveltimes residuals decreases from 0.079 to 0.053 s (Figs. 2e–2f). More details regarding the tomographic inversion are documented in Hao et al. (2024).

2.3. RF and P-coda auto-correlation

RFs that contain P -to- S converted (P_s) waves from seismic discontinuities are employed to investigate the layered lithological structure and to confine its V_p/V_s , which is highly sensitive to geothermal-related changes in fluid content and porosity. We analyze P arrivals and their coda from teleseismic events with epicentral distances of 25°–95° and magnitudes of $M_w \geq 5$ (e.g., Park and Levin, 2002). Most of the selected events originate from the east (Fig. 4a). We apply a band-pass filter with corner frequencies of 0.05–4 Hz to the teleseismic waveforms. Two

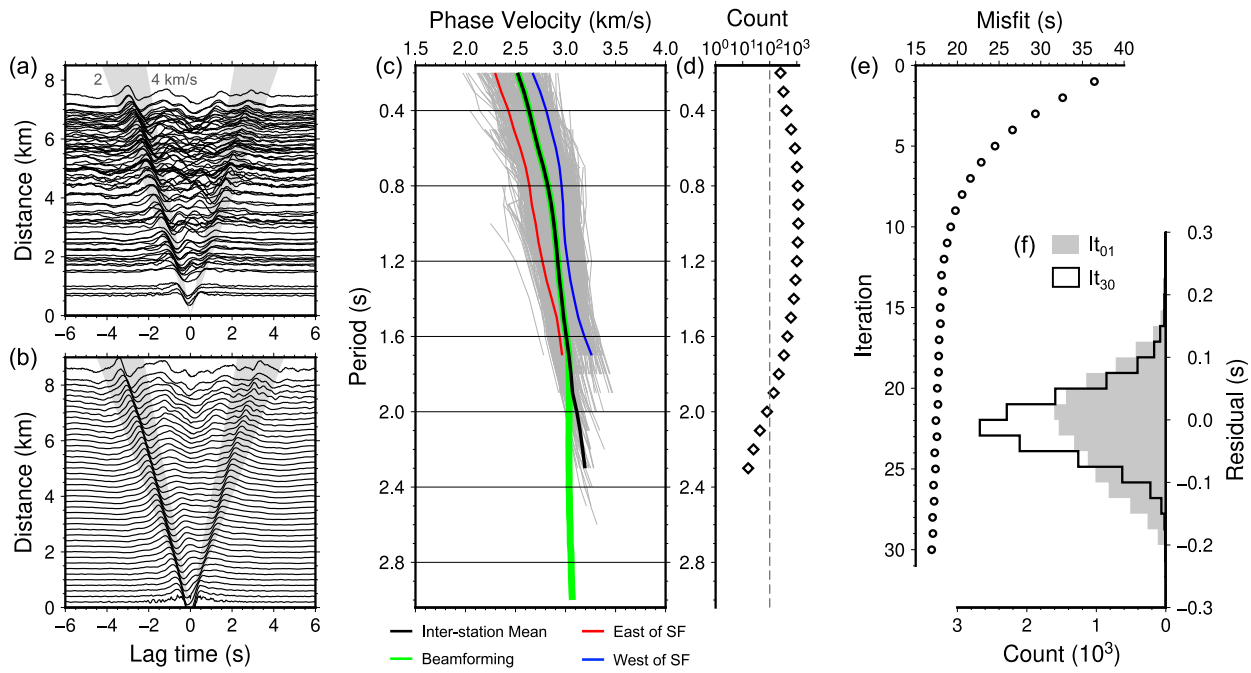


Fig. 2. Ambient noise data and inversion. (a) Cross-correlogram between one station located in the far western region and all the other stations in the Sembawang array. (b) Cross-correlogram obtained by the array-based beamforming method. In (a-b), the shaded area denotes the velocity range of 2–4 km/s. (c) Rayleigh-wave phase velocity dispersion curves. Gray curves represent discrete inter-station dispersion curves, with their mean as the black curve. We highlight the phase velocity differences between the areas on either side of the Seletar Fault (SF). The green curve denotes the average dispersion by the array-based beamforming method. (d) Number of dispersion data at 0.2–2.3 s periods. (e-f) Data misfit and residuals of ambient noise tomography. (e) Misfit reduction of the iterative surface-wave traveltome tomography. (f) Comparison of Rayleigh-wave traveltimes between the first (It_{01}) and final (It_{30}) iterations of the tomographic inversion. (For interpretation of the references to colour in this figure legend, the reader is referred to the web version of this article.)

horizontal-component seismograms are rotated to radial and transverse directions. RFs are computed using a time-domain iterative deconvolution method (Ligorría and Ammon, 1999), with a Gaussian parameter of 5.0 to preserve the high-frequency content (~2 Hz). We employ quality controls to exclude incoherent RFs, such as those with anomalously large coda amplitudes, and correct the RF amplitude to a standard ray parameter of 6.7 s^{1/2} (Xiao et al., 2021), eventually yielding 1692 valid RFs.

We also calculate auto-correlation functions (ACFs) of teleseismic and regional *P*-coda waves, following the procedure described in Pham and Tkalcic (2017), to constrain the *Vp* averaged in a specific layer (e.g., the crust). In the extraction of Moho *P* reflections, seismic events used to calculate the *P*-coda ACFs are the same as those used for RF calculation. A band-pass filter with corner frequencies of 0.05–5 Hz is applied before auto-correlation to match the dominant frequency of the RFs. We select a 45-s-long window starting 5 s before the direct *P*-wave arrival. For each station, the ACFs are computed after whitening the spectrum of the original waveform with a bandwidth of 0.5 Hz (Pham and Tkalcic, 2017). In addition to telesesimic *P*-coda ACF, we also calculated the *P*-coda ACFs from regional seismic events within epicentral distances of 0–10°. Compared with teleseismic events, these regional seismic signals contain more high-frequency components and thus can be used to extract shallow-crustal interface reflections. Here, we use a band-pass filter of 0.5–20 Hz and an empirical spectral whitening bandwidth of 3 Hz to highlight the high-frequency content.

We employ the *H*- κ stacking method (Zhu and Kanamori, 2000) to simultaneously constrain the thickness (*H*) and average *Vp/Vs* (κ) of an upper-crustal layer inferred from the RF waveforms, as well as those of the entire crust. Further incorporating *P*-coda ACF allows *Vp* to be treated as unknown (Delph et al., 2019), whereas it is fixed in the conventional *H*- κ stacking. Here only vertical-component *P*-coda ACFs are used. The radial components are also examined and found to be compatible with RFs, indicating the robustness of data processing. For a

series of *H*, κ , *Vp*, we stack the weighted RF and ACF phases (i.e., *Ps*, *PPs*, *PSs* and *Pp*) at their predicted arrivaltimes (Delph et al., 2019),

$$T_{Ps} = H \left(\sqrt{(Vp/\kappa)^{-2} - p^2} - \sqrt{Vp^{-2} - p^2} \right)$$

$$T_{PPs} = H \left(\sqrt{(Vp/\kappa)^{-2} - p^2} + \sqrt{Vp^{-2} - p^2} \right)$$

$$T_{PSs} = 2H\sqrt{(Vp/\kappa)^{-2} - p^2}$$

$$T_{Pp} = 2H\sqrt{Vp^{-2} - p^2}$$

where *p* denotes the ray parameter. The optimal set of layer parameters is obtained when the stacked amplitude reaches its maximum (with the associated uncertainties quantified by one standard deviations),

$$s(H, \kappa, Vp) = \sum_{j=1}^N \sum_{i=1}^3 \omega_i A_j + \alpha \sum_{k=1}^M A_k$$

where the first term on the right-hand side is the same as defined in the conventional *H*- κ stacking (Zhu and Kanamori, 2000) – *A_j* represents the RF amplitude in the *j*-th trace (1, 2, ..., *N*); ω_i denotes the weighting of the *i*-th phase type (i.e., *Ps*, *PPs*, *PSs*). The phase weighting parameters for *Ps*, *PPs* and *PSs* are set to be 0.6, 0.3 and 0.1, respectively, based on phase coherence (Zhu and Kanamori, 2000). *A_k* represents the theoretical *Pp* amplitude in the *k*-th trace (1, 2, ..., *M*) of the ACFs; $\alpha = \max(\sum_{i=1}^3 \omega_i A_j) / \max(A_k)$ is a weighting factor to ensure equal contribution from both datasets. To prevent the results from being dominated by data with similar ray parameters, we stack the RFs and ACFs within 0.4 s^{1/2} bins (when available). Testing different bin sizes indicates that the estimates of κ remain nearly constant, although the estimates of *H* or *Vp* can vary by up to 5 %. We note that since ACFs are of high

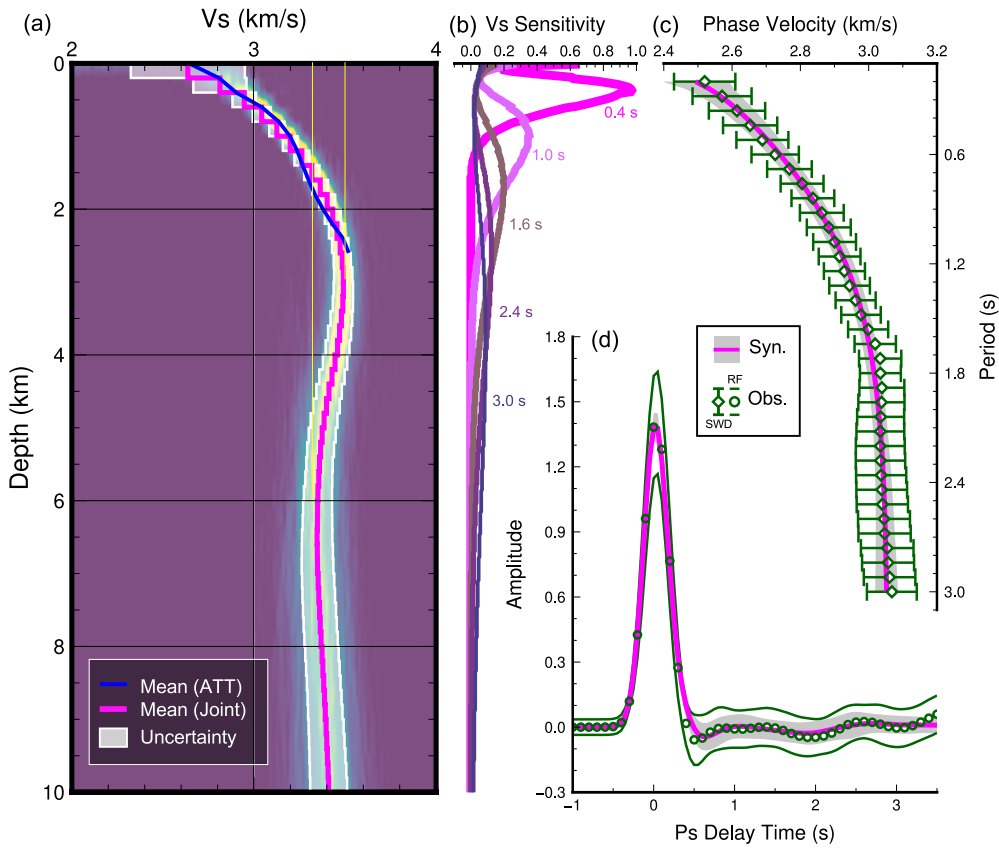


Fig. 3. Result of joint inversion of surface-wave dispersion and RF. (a) The final inverted V_s model. The purple line and the white shaded area denote the mean and one standard deviation uncertainty, respectively. The ambient 2-D histogram shows the posterior distribution of the inverted V_s . As a comparison, the blue line represents the mean V_s model from adjoint-state surface-wave tomography (Fig. 5). The two yellow lines denote a downward V_s decrease. (b) 1-D depth sensitivity kernel of Rayleigh-wave phase velocity to V_s , generated from the joint inversion model in (a). (c-d) Data fit for (c) array-averaged Rayleigh-wave dispersion and (d) array-averaged RF waveform. (For interpretation of the references to colour in this figure legend, the reader is referred to the web version of this article.)

frequencies thus generally noisy, and include more complex interference, we constrain only the regionally averaged V_p values in the RF-identified shallow-crust layer and in the entire crust. Due to the limited number of RFs at individual stations, we group the RFs in three sub-regions to examine the variations of the average H and κ in the shallow crust. The Seletar Fault divides the study area into west and east, and the SHS further separates the southeastern region from the northeastern region. In this step, to ensure a stable estimation, we perform the conventional $H\text{-}\kappa$ stacking, with V_p fixed to the ACF-confined regional averages of 5.5 km/s for the upper crust and 6.1 km/s for the entire crust.

To generate a depth-domain crustal conversion image while improving spatial resolution, we migrate RFs onto a grid with horizontal dimensions of 0.1 km and vertical dimensions of 0.2 km (Kind et al., 2002). All the amplitudes located in the same grid cell within 2 km on either side of a designated profile are then stacked. Note that to avoid image distortion, no smoothing filter is applied. We construct a 1-D velocity model for time-to-depth conversion. In the upper 10 km depth, we use the local V_s model obtained through the Bayesian joint inversion (Section 2.4), with V_p converted using the average V_p/V_s derived by the $H\text{-}\kappa$ stacking. The deeper structure is represented by the global IASP91 model (Kennett and Engdahl, 1991). Nonetheless, due to the lack of a high-resolution 3-D crustal velocity model, the obtained images reflect apparent depths of the RF phases rather than true depths. Subsequently, we pick the apparent depths corresponding to the maximum amplitude of coherent RF phases from the migrated images, with their uncertainties quantified by 100 bootstrapping iterations (Efron, 1992). In each iteration, we randomly select 80 % of RF traces from the original database, without duplication. We then perform RF

migration and phase picking using the resampled data. Recognizing that uncertainty estimation using bootstrapping methods may be underestimated, we set the picking errors to be two standard deviations of the picked depths across all iterations.

2.4. Probabilistic joint inversion

We explore the complementary sensitivities of surface-wave dispersion and RF to V_s structure through a Markov Chain Monte Carlo joint inversion (Guo et al., 2016; Mosegaard and Tarantola, 1995). Due to the relatively high level of urban noise (Fig. S1) and the localized scale of our study area, we invert for a regional-average model using the array-averaged measurements, rather than station-wise results. To enhance sensitivity at greater depths (e.g., > 5 km), we measure phase velocities at extended periods of 2–3 s using a beamforming method (Qin et al., 2022) and combine them with the stack of all the inter-station dispersion curves at 0.2–2 s periods (Fig. 2c). Meanwhile, RFs are linearly averaged and then truncated at 3.5 s after P arrival to avoid complexities associated with the Moho. The uncertainties of both the dispersion and RF data are quantified by one standard deviation of the associated measurements. The 1-D isotropic V_s model in the upper 20 km depth is represented by two major layers. We perturb 9 free model parameters, including 8 B-splines (4 in each layer) that define the V_s structure and the depth to the upper-layer base (See Table S1 for detailed model space settings). Since both datasets are primarily sensitive to V_s , V_p is scaled based on the V_p/V_s estimated by the $H\text{-}\kappa$ stacking, and density is derived by an empirical relationship (Brocher, 2005). The objective function ϵ that quantifies the difference between measured and simulated data is defined as:

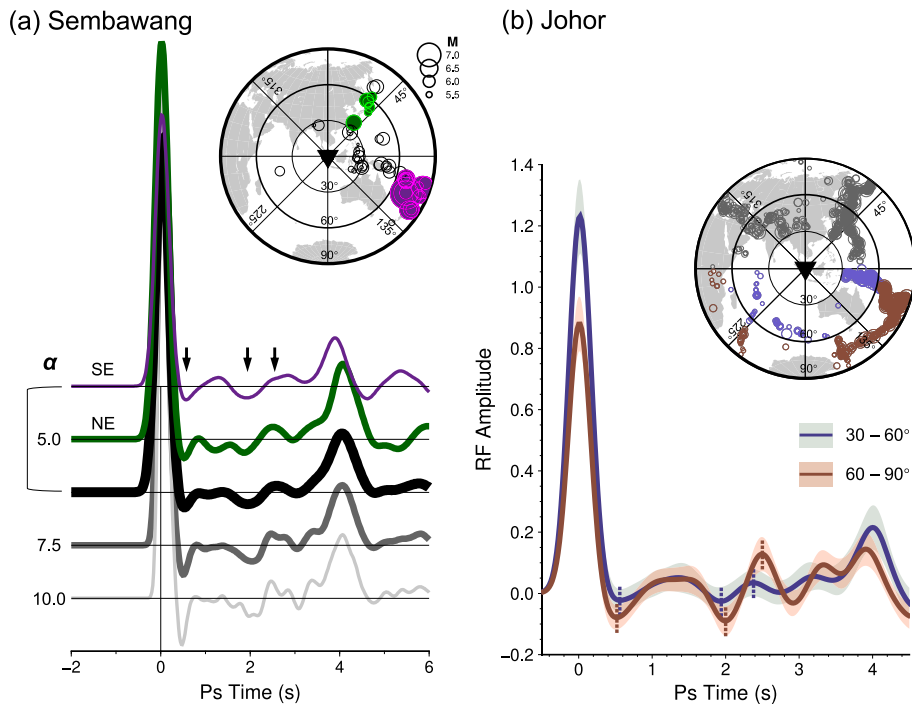


Fig. 4. Stacked RFs from (a) the Sembawang and (b) the Johor datasets. In (a), the upper panel displays the distribution of teleseismic events used for RF computation. The bottom panel shows stacked RFs. The upper two stacks use events from different distances and back-azimuths, as indicated in the event distribution map. The bottom three stacks use all the available RFs but with different Gaussian parameters (α) of 5.0, 7.5 or 10.0. The three intra-crustal RF phases discussed in the text are highlighted. (b) Slowness dependency of the RFs from the Johor dataset. The upper panel displays the distribution of teleseismic events available for RF computation; only those from the south are used. The blue and red lines (with shades) represent stacked RFs (with one standard deviation uncertainties) in the epicentral distances of 30–60° and 60–90°, respectively. The three intra-crustal RF phases are marked. We find that with increasing epicentral distance, the 0.5-s RF phase arrives earlier, similar to the behavior of direct conversions like the Moho conversion. By contrast, the 2- and 2.5-s phases arrive later with increasing distance. Additionally, amplitudes of the latter two phases exhibit a positive correlation with the 0.5-s phase amplitude. (For interpretation of the references to colour in this figure legend, the reader is referred to the web version of this article.)

$$\epsilon(\mathbf{m}) = \sum_{j=1}^2 \omega_j \sum_{i=1}^{N_j} \frac{\{g_{j,i}(\mathbf{m}) - d_{j,i}\}^2}{\delta_{j,i}^2} + \frac{\omega_s}{l} \sum_{k=1}^{L-1} \frac{\{\text{sign}(\beta_k - \beta_{k+1})\}(\beta_k - \beta_{k+1})}{0.1}$$

where the first term on the right-hand side is the summation of the squared misfit between model prediction $g(\mathbf{m})$ and observed data d , weighted by the data uncertainties δ over all the data points N . $j = 1, 2$ refers to surface-wave dispersion and RF, respectively. The second right-hand term is a smoothing term designed for penalizing complicated models, with 0.1 km/s for normalization (e.g., Bai et al., 2023; Xiao et al., 2021). β_k indicates the V_s of the k -th sublayer from the surface as models being discretized by fine layers with a constant thickness of 0.2 km. L and l are the total number of sublayers and the number of sub-layers where V_s decreases downwards, respectively. The weighting factors (i.e., $\omega_1, \omega_2, \omega_s$) are chosen equally to 1.0 because we mean to fit both datasets with no priority while restraining model complexity. We sample the model space following the strategy of Bai et al. (2023). In the initial burn-in stage, 20,000 models are randomly drawn from uniform distributions; in the subsequent post burn-in stage, 40,000 models are constructed, with the proposal distribution calibrated every 4000 iterations. Eventually, we select an ensemble of 600 models from all the accepted model in the Markov chain to represent the final model and its uncertainty.

3. Results

Ambient noise tomographic images reveal clear V_s heterogeneities in the upper crust (Fig. 5). At <1 km depths, the northwest-southeast

oriented Seletar Fault clearly separates a faster western zone from a slower eastern zone, with a mean V_s difference of ~ 0.15 km/s (Figs. 5a-5b). This feature can be observed directly from the raw dispersion (Fig. 2c). At >1 km depths, the low V_s east of the Seletar Fault persists but becomes more pronounced south of the SHS beneath the Yishun District. There, the V_s is decreased by up to 12 % relative to depth averages (Figs. 5c-5d). Checkerboard tests suggest that our tomographic model, with a lateral resolution of ~ 2 km, can robustly resolve the features under discussion (detailed in Section 4.1).

In the RF waveforms, we identify two negative phases at ~ 0.5 s and ~ 2 s, and a less pronounced positive phase at ~ 2.5 s (Fig. 4). These three phases likely represent the P -to- S phase, converted from an upper-crustal interface with a downward impedance decrease, and its multiples (detailed in Section 4.1). We map the 0.5-s negative phase to space and observe evident spatial variations. For instance, a sudden increase of ~ 2 km in the apparent depth of this negative phase is found in the migrated RF profile immediately beneath the surface projection of the Seletar Fault (Fig. 6a). Meanwhile, we find that the 0.5-s phase is mapped at greater apparent depths up to ~ 8 km and overall weaker in amplitude beneath Yishun in the southeast than beneath the rest of the study area (Figs. 6b & 7a), in agreement with the lower V_s there resolved by ambient noise tomography (Figs. 5c-5d). Moreover, the V_p/V_s averaged in the identified upper-crustal layer beneath Yishun is estimated to be 2.1 ± 0.24 (Fig. 7b). This estimate, however, is considerably higher than those of the 1.64 ± 0.14 and 1.71 ± 0.16 beneath the western and northeastern study areas, respectively (Figs. 7c-7d). RF modeling also supports a higher V_p/V_s beneath Yishun (Fig. S4). Compared to V_p/V_s , the layer thicknesses beneath the three sub-regions show less pronounced variations, ranging from ~ 3.8 to ~ 4.3 km. In addition, the estimated thickness and average V_p/V_s in the entire crust are 31.5 ± 0.3

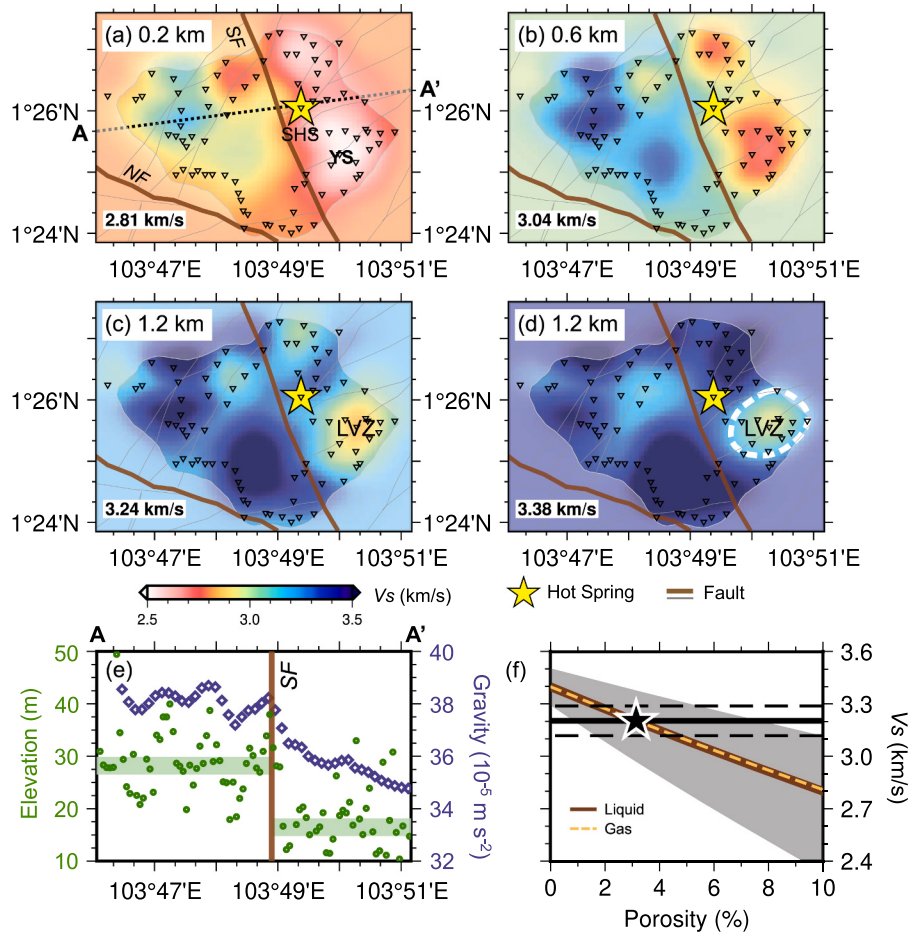


Fig. 5. Ambient noise tomographic model. Horizontal cross-sections of the tomographic V_s model at representative depths of (a) 0.2, (b) 0.6, (c) 1.2 and (d) 2.0 km are shown. Each subfigure shows the V_s distribution, with the mean value given at the bottom-left corner. Areas with limited resolution are shaded. The dashed line in (a) denotes the elevation and gravity profile shown in (e). LVZ in (c-d) denotes the low- V_s anomaly at >1 km depths, with white circle denoting the 3.2 km/s contour. The SHS, seismic stations, major and minor faults are superimposed. NF – Nee Soon Fault; SF – Seletar Fault; YS – Yishun District. (e) Elevation and gravity across the Seletar Fault (in brown), both showing district variations. The thick green lines indicate the average elevations on either side of the fault. (f) Porosity estimation in granitic rocks based on the relations by Toksöz et al. (1976) and the parameters in Table S2. The dark- and light-brown lines represent the V_s -porosity relationships given a liquid or gaseous pore fluid, respectively. The gray shaded area indicates the uncertainties due to pore aspect ratio and V_s . The black solid and dashed lines mark the assumed V_s in porous rocks and its uncertainty, respectively. The star denotes the favored porosity of $\sim 3.2\%$. (For interpretation of the references to colour in this figure legend, the reader is referred to the web version of this article.)

km and 1.72 ± 0.2 , respectively, indicative of a felsic continental nature (Figs. 8a-8b) (Christensen, 1996; Christensen and Mooney, 1995).

An overview of the isotropic velocity structure from surface to 10 km depth beneath the SHS and its vicinity is obtained via the Bayesian joint inversion of Rayleigh-wave dispersion and RF (Fig. 3). The average V_s exceeds 3 km/s at ~ 500 m depth and gradually increases to ~ 3.5 km/s at ~ 3 km depth. Within the depth range of ~ 3.5 –5 km, a ≤ 0.3 km/s V_s decrease is observed, suggesting the presence of a faster shallow-crustal layer than the underlying basement.

4. Discussion

4.1. Result robustness

Checkerboard tests are carried out to assess the spatial resolution of our tomographic V_s model (Fig. S3). We use a combination of sine functions to design 3-D gradually changing velocity anomalies relative to the initial 1-D model built for inversion (Hao et al., 2024; Tong, 2021). The dimensions of these anomalies are defined to ensure that each anomaly checker can be adequately sampled by at least three inversion nodes. We prepare two sets of checkers with horizontal widths of 2 and 2.5 km and assign two layers, with zero amplitude anomalies at

1 km depth. The maximum perturbation of the input anomalies is 15 %, comparable to the magnitude in the inverted model. We then calculate synthetic Rayleigh-wave phase traveltimes in this input model, with random Gaussian noise with zero mean and 0.1 s standard deviation added to the forward calculation. The inversion is performed using the same parameters as for the real data. The results show that our model can accurately recover anomalies with a lateral size of 2.5 km, while further reducing the anomaly size may result in smearing (e.g., at the western end of the study area) and slight underestimation in anomaly amplitude (Figs. S3m-S3p). We emphasize that the identified key features, including the velocity contrast across the Seletar Fault and a low-velocity zone southeast of the SHS (Fig. 5), are robust. We further evaluate the model uncertainty through bootstrapping (Efron, 1992). To achieve this, we randomly draw 80 % of all dispersion measurements without replacement and repeat this process 100 times. Tomography is performed for each of the 100 down-sampled datasets, with the two standard deviations of all the resulting V_s models used to quantify the model uncertainty. The V_s uncertainties are generally within 0.04 km/s across most of the study area, which is considerably small, although uncertainties can exceed 0.2 km/s near the array borders due to inadequate data coverage (Fig. S5).

The strongest phase in the RF wave trains from the Sembawang data

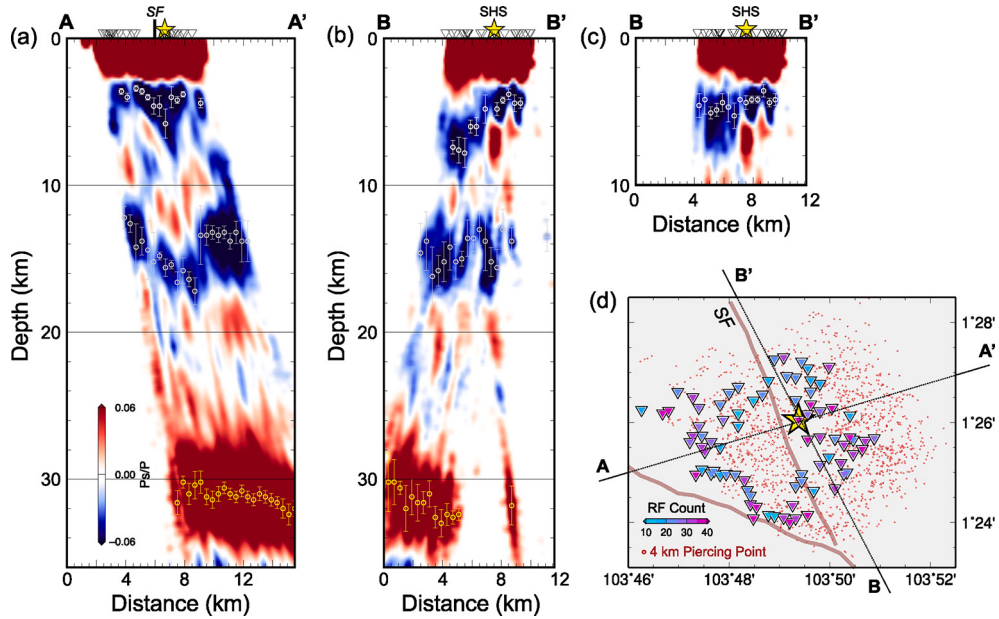


Fig. 6. RF depth migration results. RFs are converted to the depth domain (a) across and (b-c) along the strike of the Seletar Fault. The SHS, the Seletar Fault (SF) and the seismic stations close to the profile are projected on top. Dots and error bars track the strongest amplitudes of the identified major RF phases along the profiles and their associated uncertainties, respectively. (c) is built along the same profile as (b) except that the Vs south of the SHS in the Yishun shallow crust is reduced by 10 %, to account for the identified low-velocity anomaly. (d) RF counts at individual stations and piercing points at 4 km depth, where an upper-crustal discontinuity is likely present. Dashed lines represent the surface locations of the two profiles AA' and BB' shown in (a) and (b-c), respectively.

is the direct P phase, which arrives at zero-lag time without noticeable delay (median arrival time at 0.02 s; Fig. 2a). This suggests minimal sedimentary cover in the study area, if any, with a thickness much smaller than the dominant wavelength of the RF data (~ 1 km). The shallow boreholes near the SHS encounter a soil layer of 20–50 m, underlain by weathered granite (Zhao et al., 2002). These observations align with regional geology, indicating that our study area is predominantly floored by the BTG, while younger sedimentary sequences of the Jurong Formation and Kallang Formation are located further east and west, respectively (Fig. 1b) (Dodd et al., 2019). Consequently, the RF waveforms in this region experience little sedimentary effect. Following the direct P , a negative phase at ~ 0.4 – 0.8 s is identified at 74 out of the 80 stations (92.5 %) (Fig. 7a) and is interpreted as an intra-crustal downward impedance decrease. This phase, along with the subsequent phases at ~ 2 and ~ 2.5 s, is stable with no obvious time shift across different frequency bands, indicating that they are real signals rather than noise or side lobes (e.g., Chen et al., 2009). Moreover, the slowness dependency of a RF phase can effectively discriminate direct conversions from reverberations. The limited number of RFs from the 4-month observation period and the high level of urban noise, however, restrict reliable slowness analysis. Fortunately, the three intra-crustal RF phases are also observable at a long-term permanent station located ~ 40 km north of our study area in Johor, Malaysia (Fig. 1a). Using the data from Johor, we analyze RFs from large-magnitude events of $M_w > 6$ (for high signal-to-noise ratio) with a back-azimuth range of 90–270° (for gaining insight into the subsurface structure nearer to Singapore). Similar to direct Ps conversions from the Moho, the 0.5-s negative phase arrives earlier as the epicentral distance increases, while the 2- and 2.5-s phases show the opposite behavior (Fig. 2b). Combining this observation with the positive amplitude correlation of the 0.5-s negative phase with the 2- and 2.5-s phases, and considering the Ps - P and PSS - PPs time intervals, we conclude that the 2- and 2.5-s phases are multiples of the 0.5-s phase.

Our new seismic images are compatible with existing geological and geophysical knowledge in Singapore (e.g., Gillespie et al., 2019; Lythgoe et al., 2020; Macpherson et al., 2013; Zhao et al., 2002). The relatively high average V_s , exceeding 3 km/s at a shallow depth of ~ 500 m

(Fig. 3a), can be attributed to the presence of the BTG, composed of high-velocity intrusive rocks likely departing from the paleo-Tethys subducted slab (Gillespie et al., 2019; Metcalfe, 2013). The array-average V_p estimated by $H\text{-}\kappa$ stacking (Figs. 8b & 8f) also agree with typical V_p of granitic rocks in the crust (e.g., Christensen, 1965). At <1 km depths, the area east of the Seletar Fault exhibits lower V_s compared to the west (Figs. 5a–5b). Since there is no *in-situ* deep log within the region, validating this velocity contrast is more practical by considering rock density, as seismic velocity generally correlates positively with density (Brocher, 2005; Christensen and Salisbury, 1973). High-resolution free-air gravity data show a prominent eastward decrease across the Seletar Fault (Hirt et al., 2013), in line with the lower upper-crustal V_s observed in the east (Fig. 5). This contrast also aligns with former petrographic analyses, which identify the Seletar Fault as the boundary between two plutons within the BTG – the eastern Simpang Pluton, primarily composed of synegranite with U–Pb zircon ages of 231–229 Ma, and the western Dairy Farm Pluton, composed of monzogranite with slightly older zircon ages of 246–235 Ma (Fig. 1b) (Gillespie et al., 2019). This lithological variation across the Seletar Fault may partially explain the observed V_s contrast. Beyond the uppermost crustal structure, a Ps phase from the Moho seen at ~ 4 s in the RFs, along with its multiples at ~ 13.5 and ~ 17.5 s, indicates a local crustal thickness of ~ 31.5 km predicted by both RF depth migration and $H\text{-}\kappa$ stacking (Figs. 6 and 8). This value agrees with the previous estimates of 30–32 km beneath mainland Singapore (Lythgoe et al., 2020; Macpherson et al., 2013).

4.2. Shallow-crustal geothermal reservoir southeast of the SHS

Rayleigh-wave dispersion and RFs collectively reveal anomalous low- V_s and high- V_p / V_s structures in the shallow crust southeast of the SHS beneath the Yishun District (Figs. 5 and 7). We link this velocity anomaly to a probable shallow-crustal geothermal reservoir.

Previous studies indicate that seismic velocity can be influenced by a range of factors, including lithology, temperature, crack fraction and saturation conditions (e.g., Mavko et al., 2020). Of these factors, lithology is probably the most fundamental in the shallow crust

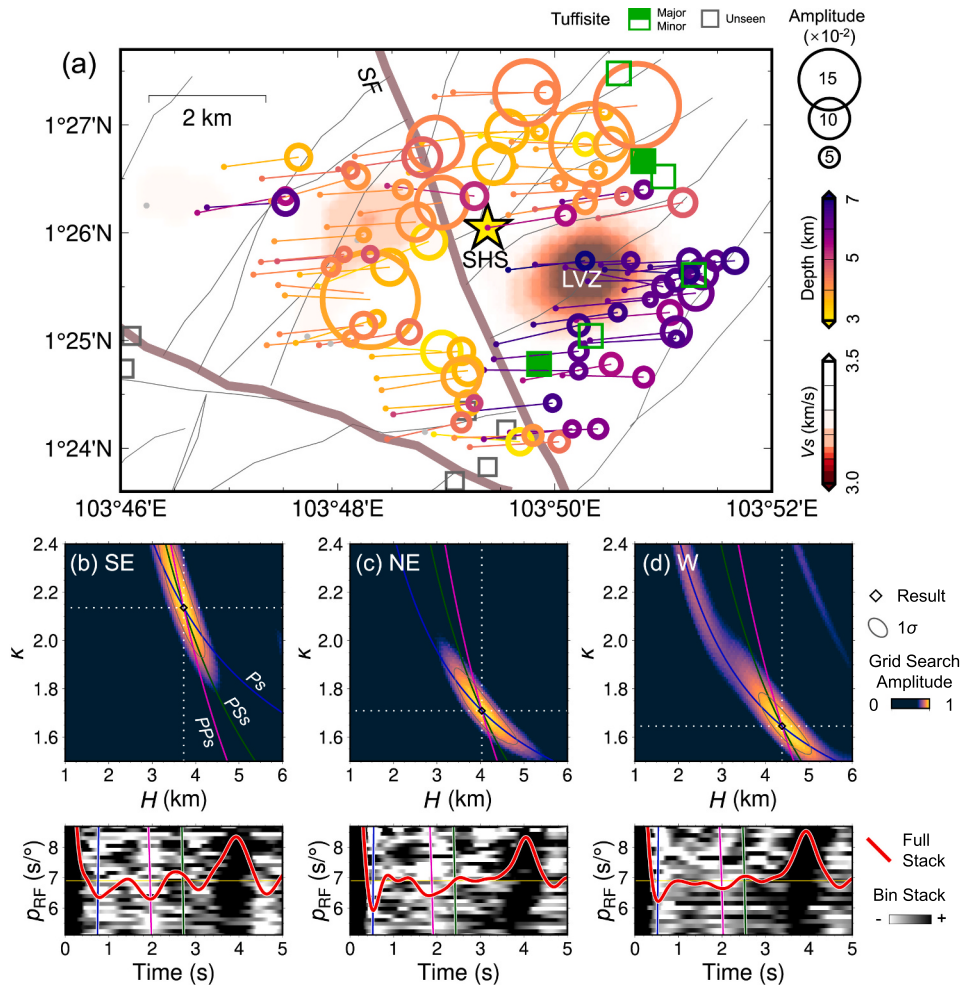


Fig. 7. Characteristics of the shallow-crustal RF negative phase and sub-regional $H\text{-}\kappa$ stacking. (a) Shallow-crustal negative RF phases at stations. For each station (indicated by a dot), the strongest negative phase in the upper 10 km is identified in the stack of depth-domain RFs. The amplitude and apparent depth of this phase are represented by a circle, placed upon the average piercing point at the depth where the negative phase is picked. Stations with unclear or absent shallow-crustal negative phases (amplitude > -0.02) are shown in gray. Borehole locations (Gillespie et al., 2019) are marked by squares, where green-filled or green-outlined denote major or minor tuffsite presence, respectively, and gray indicates the absence of tuffsites. The tomographic low-velocity zone (LVZ) at 2 km depth (Fig. 5d) is also included for comparison. (b-d) $H\text{-}\kappa$ stacking using the shallow-crustal phases from stations in (b) southeastern, (c) northeastern and (d) western sub-regions. In each subfigure, the optimal H and κ combination and its uncertainty are shown in the upper panel; the corresponding RF waveforms are shown in the lower panel. Theoretical phase arrivaltimes computed using the optimal H and κ are superimposed. (For interpretation of the references to colour in this figure legend, the reader is referred to the web version of this article.)

(Christensen and Mooney, 1995). The composition difference between the Dairy Farm Pluton and the Simpang Pluton (Gillespie et al., 2019) may account for the tomographic V_s contrast at <1 km depths on either side of the Seletar Fault (Figs. 5a-5b). However, the area east of the Seletar Fault is uniformly underlain by the Simpang plutonic rocks (Fig. 1b), which makes it difficult to attribute the lower V_s in the southeast, compared to the northeast, to a lithological genesis alone. An alternative explanation could be increased temperature, which typically reduces seismic velocity (Mavko et al., 2020). Previous numerical modeling predicts that groundwater temperatures beneath the SHS and its surroundings range in $\sim 50\text{--}200$ °C within the upper 5 km (Tjiawi, 2013). This temperature variation may account for a minor reduction in V_p or V_s by less than 0.1 km/s (Kern and Richter, 1981; Spencer Jr. and Nur, 1976), while the observed V_s in the low-velocity zone decreases by up to ~ 0.3 km/s compared to the surrounding area. Therefore, additional factors are at play.

The presence of cracks and fractures typically decreases both V_p and V_s (O'Connell and Budiansky, 1974). Gillespie et al. (2019) report that the BTG is featured by highly irregular fractures with filling of shattered intrusive rocks (or tuffsites), which are thought to have been formed by

forceful injection of high-pressure hydrothermal fluids, triggered by rapid crustal rebound following slab breakoff (Gillespie et al., 2019; Metcalfe, 2013; Oliver et al., 2014). The identification of several major and minor tuffsites in the anomalous Yishun region (Figs. 7a & 9a) indicates extensive fracturing there, which significantly weakens rocks (Kolzenburg et al., 2012) and may contribute to the lowered V_s . In the same region, the V_p/V_s averaged in the shallow crust is estimated at ~ 2.14 , much higher than the observed ≤ 1.71 in the rest of the study area. These latter values are more consistent with the formerly reported range of 1.65–1.70 for the granite-granodiorite rocks under upper-crustal conditions (Christensen, 1996; Fliedner et al., 2000). A plausible implication for the elevated V_p/V_s is that the tuffsite-filled cracks are saturated at depth, leading to increased bulk V_p/V_s (O'Connell and Budiansky, 1974). To quantitatively estimate the fluid fraction, we make use of the scattering theory (Toksoz et al., 1976), given the elastic properties of the solid matrix and pore fluids of rocks (Table S2), as well as pore geometry. Based on field observations (Lee and Zhou, 2009; Leslie et al., 2019), we assume that cracks are the predominant pore geometry in the BTG, with a plausible pore aspect ratio ranging from 0.05 to 0.2. The favored model setup results in a fluid fraction of $\sim 3.2\%$,

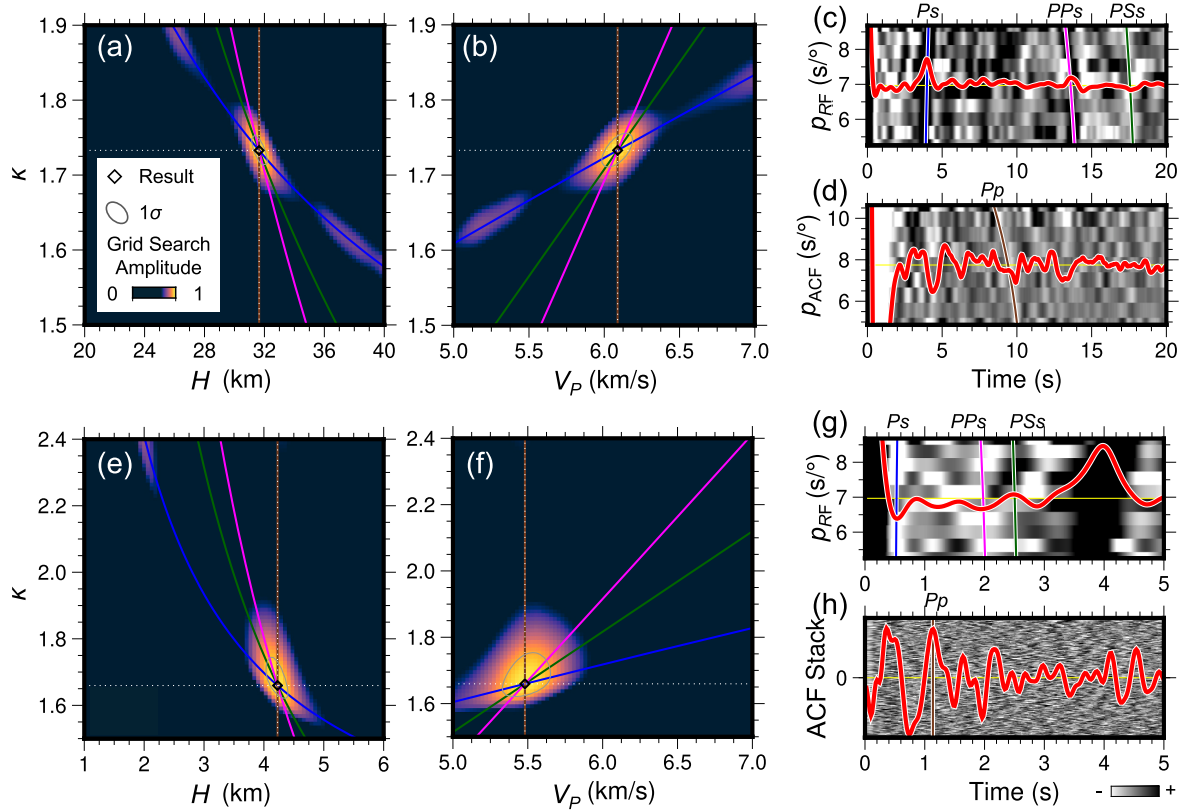


Fig. 8. Array-averaged H - κ stacking, with V_p as an unknown. (a-d) present results for the entire crust. (a-b) show the grid search results for layer thickness, layer-average V_p /Vs and layer-average V_p . (c-d) show the stacked (red line) and bin-stacked (colormap) RFs (c) and P -coda ACFs (d). Theoretical phase arrivaltimes computed using the optimal H , κ and V_p are superimposed. (e-h) are similar to (a-d) but the results for the shallow-crustal layer. In (h), as the regional earthquakes used for ACF computation possess similar ray parameters, the background colormap shows individual ACFs sorted by distance. (For interpretation of the references to colour in this figure legend, the reader is referred to the web version of this article.)

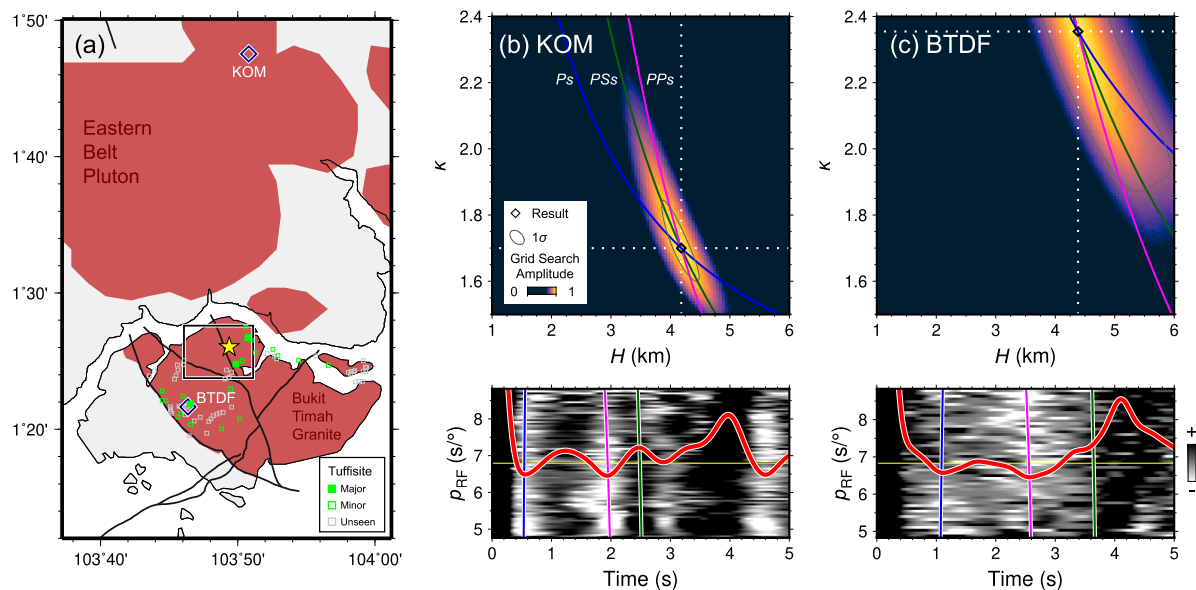


Fig. 9. H - κ stacking results using data outside of the study area. (a) Map showing the two permanent stations (diamonds) outside of the study area (box). Squares represent locations of the boreholes in East Singapore (Gillespie et al., 2019). The star denotes the SHS. Black lines denote major faults in the region. (b-c) H - κ stacking results in the shallow crust beneath station (b) KOM in Johor, Malaysia and (c) BTDF at the Bukit Timah Hill in Central Singapore. In each subfigure, the upper and bottom panels show the grid search result and RF waveforms. See Fig. 7 for more details.

which could fully account for the observed low-V_s anomaly beneath Yishun (Fig. 5f). This estimate may be conservative, as we use the average V_s outside of the low-V_s zone to represent intact granite, while the entire BTG is believed to be fractured to varying degrees (Lee and Zhou, 2009). In short, we infer that the low-V_s and high-V_p/V_s anomalies in the shallow crust beneath Yishun are associated with extensive, fluid-filled cracks, facilitating the development of a geothermal reservoir. Geothermal reservoirs developed in fractured granitic rocks have been reported in other non-volcanic sites, e.g., north of the study area in Malaysia (Baioumy et al., 2015) and Thailand (Amatyakul et al., 2023). We also speculate that tuffisites could be an indicator of geothermal potential in the BTG. Outside of our study area, a correlation between high shallow-crustal V_p/V_s of ~2.3 and major tuffisites is found at the Bukit Timah Hill (Fig. 9), potentially indicating the existence of additional reservoirs. Further investigations and additional data are needed to support the hypothesis.

We observe that the proposed shallow reservoir is located east of the Seletar Fault. This fault may have been active during the Early Cenozoic, which is posterior to the emplacement of the BTG, but is likely to have become dormant since the Neogene (Gillespie et al., 2019). The RF depth profile normal to the Seletar Fault shows an evident deepening of the upper-crustal discontinuity immediately beneath the surface fault trace (Fig. 6a), suggesting a vertical extent of the fault to at least 4 km depth. This scenario is roughly replicated through a 2-D waveform modeling (Fig. S6) (Li et al., 2014). Although the RF profile appears to hint at an eastward dip of the Seletar Fault, this is likely an artifact, given that almost all the events originate from the east. The modeling result using a vertical dipping angle fits the observation fairly well (Fig. S6), reinforcing previous findings that most brittle faults in the bedrock of Singapore are steeply dipping (Leslie et al., 2019; Zhao et al., 2002). Notably, the SHS is positioned on the northwestern edge of the reservoir, adjacent to the Seletar Fault (Fig. 5). We speculate that the Seletar Fault, as a prime weak zone in the shallow crust, may play a key role in transferring hot fluids up to the hot spring, aligning with the fault-assisted origin proposed for the SHS (Zhao et al., 2002). In addition to the major Seletar Fault, a series of northeast-southwest striking minor faults is present throughout the study area (Lee and Zhou, 2009; Leslie et al., 2019; Zhao, 1998), likely influenced by local stress (Oliver et al., 2011). The modern urban landscape of Singapore restricts fault exposures, indicating the potential existence of blind faults. We suspect that some northeast- to east-trending minor faults may prevent the shallow geothermal reservoir from extending further north of the SHS. In this case, the SHS emerges at the intersection of multiple faults, which is the most probable location for hot springs to crop out (Curewitz and Karson, 1997). Due to the limited array aperture, our results provide little constraint on the extent of this reservoir toward the southeast, which will be addressed by future studies with extended data coverage. Nevertheless, our speculation about tuffisites as indicators of geothermal resources, though pending further validation, implies that the proposed shallow reservoir might extend further east, where significant tuffisites have been identified (Fig. 9).

4.3. Boundary between the BTG and the metasedimentary basement

Our research reveals a distinct seismic discontinuity, characterized by a downward decrease in V_s of $\sim 0.2 \pm 0.1$ km/s and apparent depths of $\sim 4\text{--}8$ km, across the study area (Figs. 3, 6–7). While shallow-crustal velocities typically increase with depth due to changes in mineral/chemical composition or porosity (e.g., Bai et al., 2023; Xiao et al., 2021), the observed V_s downward decrease beneath the SHS and its surroundings is puzzling.

Investigating the extent of the shallow-crustal discontinuity can provide insights into its origin. We find that this interface is not a localized feature but extends beyond our study area. A similar negative RF phase immediately following the direct P phase is detected at two adjacent permanent stations – one at the Bukit Timah Hill west of the

study area and the other to the north in Johor, Malaysia, both floored by plutonic rocks (Fig. 9). We are unable to identify this negative RF phase at other open-access stations nearby, likely due to interference from sedimentary cover and/or fault scatterers (Fig. 1b). The observed shallow-crustal V_s discontinuity might exist beneath much of East Singapore, where the BTG crops out, as inferred from a recent nationwide nodal experiment (Lythgoe et al., 2020). However, the uneven data distribution in the previous study obscures clear identification of the extent of this interface. Nevertheless, these observations imply a possible spatial correlation of the observed negative RF phase with the BTG, and potentially its parent unit, the Eastern Belt.

We propose that the upper-crustal V_s discontinuity observed beneath the study area likely marks the base of the BTG. This is supported by both surface geology and our V_s inversion (Fig. 3), suggesting that the higher-velocity layer above the discontinuity comprises primarily granitic rocks (Gillespie et al., 2019; Zhao et al., 2002). The apparent depth to the V_s discontinuity is ~ 4 km across most of study area but increases to >6 km beneath Yishun (Figs. 6b and 7a). This apparent deepening is likely due to the presence of the low-V_s anomaly at shallower depths (Fig. 6c), while a uniform 1-D model is adopted for RF migration (See Section 2.3). The estimated ~ 4 km thickness of the BTG nowadays aligns with the typical thickness of large granitic plutons, which generally do not exceed 10 km, depending on the age and volume of intrusions (Petford et al., 2000). Meanwhile, the most probable basement rocks below the discontinuity and underlying the BTG are the Carboniferous metamorphosed sedimentary deposits of the Sajahat Formation (Pan et al., 2018). Field investigations confirm that the Sajahat Formation has been significantly altered by contact metamorphism during the emplacement of the BTG (Lee and Zhou, 2009). This formation is also the oldest rock unit in Singapore, cropping out east of the study area (Fig. 1b). Notably, the Sajahat Formation comprises mainly of regionally metamorphosed quartz-rich sandstone and mudstone (Dodd et al., 2019; Lee and Zhou, 2009), which inherently have lower V_s than the overlying granitic rocks (Christensen, 1996; Mavko et al., 2020). This should explain the downward V_s decrease revealed by our data. However, alteration processes, such as the conversion from quartz sandstone ($V_s < 3.5$ km/s) to quartzite ($V_s \geq 4$ km/s) in upper-crustal environments (Christensen, 1996; Lee and Zhou, 2009; Mavko et al., 2020), can substantially elevate the velocities of the Sajahat Formation basement rocks. Thus, lithology alone may not fully account for this downward velocity decrease.

We again consider porosity to further explain the lowered V_s at depths greater than ~ 4 km. This is due to that sandstone, which is the main composition of the metasedimentary basement, typically possesses a higher permeability of up to $\sim 10^{-11}$ m², compared to granite, with a range of $\sim 10^{-17}\text{--}10^{-14}$ m² (Brace, 1980; Zhao et al., 2002). To quantitatively assess the influence of porosity on velocity reduction in sandstone, we approximate the V_s of sandstone using the empirical equation by Eberhart-Phillips et al. (1989),

$$V_s = 3.70 - 4.94\phi - 1.57\sqrt{C} + 0.361(P_e - e^{-16.7P_e})$$

where ϕ and P_e represent porosity and effective pressure, respectively. For simplicity, the clay content (C) incorporated into the V_s estimation accounts for the presence of mudstone in the Sajahat Formation. Assuming a typical clay content of 5 % (Mavko et al., 2020), the observed V_s of $\sim 3.3 \pm 0.1$ km/s at a depth of 4–5 km (Fig. 3a) can be explained by a porosity ranging in $\sim 10.7 \pm 2$ %. This porosity estimate is comparable to the previous estimates of 10–12 % for porous sandstone at similar depths (Boggs Jr, 2009). Moreover, the rock pores are probably filled with fluids, as otherwise they would tend to collapse under the high pressure at ≥ 4 km depths. Since V_s varies little between liquid- and gas-filled pores (e.g., Fig. 5f), the exact nature of the pore fluids remains to be determined.

In summary, we suggest that the lithological contrast between the BTG and the lower metasedimentary basement of the Sajahat Formation,

as well as the considerable porosity of the metasediments, collectively contribute to the development of the shallow-crustal seismic discontinuity beneath North Singapore.

4.4. Inferred geothermal system beneath North Singapore and its implications

Our results, combined with prior geological and geophysical knowledge, suggest a plausible scenario for the geothermal process beneath North Singapore (Fig. 10). In the study area, mass flow simulations show that meteoric water from high-altitude regions (e.g., Central Singapore) can penetrate the plutonic rocks of the BTG to depths of 3–5 km (Tjawi, 2013), where the shallow-crustal V_s discontinuity is detected. As a result, a deep aquifer may potentially form within the permeable sandstone of the Sajahat Formation basement. The high intensity of tropical rainfall in Singapore provides a steady supply of freshwater for groundwater recharge. The heated aquifer fluids at depths would then ascent due to buoyancy, using faults and cracks as channels (Zhao et al., 2002). The granitic rocks in the shallow crust beneath the Yishun District may be highly fractured, which promotes the influx of fluids from the deeper aquifer. This is supported by the less sharp shallow-crustal discontinuity and the atop low- V_s and high- V_p/V_s anomalies observed beneath Yishun (Figs. 5 & 7). Additionally, the lower altitude east of the Seletar Fault compared to the west also creates an essential hydraulic head contrast for fluid discharge (Fig. 5e) (Stober and Bucher, 2021). Thermal expansion of fluid-filled pores in wet rocks may promote further fracturing in the Yishun upper crust (Paquet et al., 1981). Eventually, a shallow-crustal reservoir forms beneath Yishun, supplying hot water to the nearby SHS. The proposed geothermal reservoir is located at depths of $< \sim 4$ km, consistent with the geochemical estimate of ~ 3.8 km, derived using a geothermometer temperature of ~ 160 °C at the SHS, a geothermal gradient of ~ 35 °C/km and an average surface temperature of 27 °C in Singapore (Oliver et al., 2011; Tjawi, 2013).

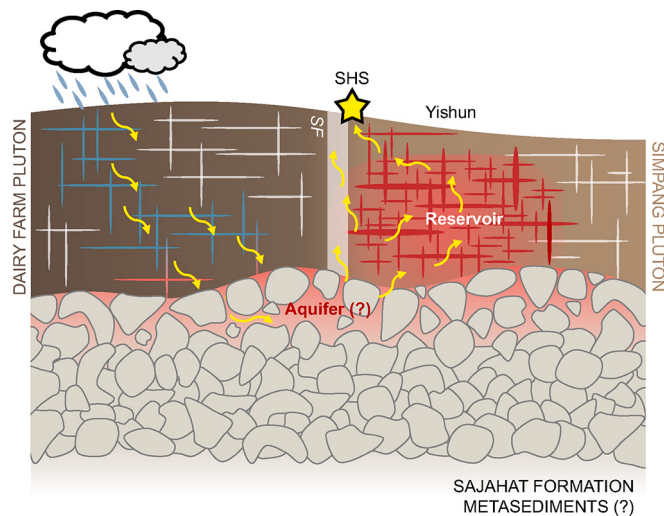


Fig. 10. Sketch summarizing the key findings of this study. We observe a low- V_s and high- V_p/V_s zone in the upper crust beneath the Yishun District, likely associated with a shallow geothermal reservoir, and a seismic discontinuity marked by a ~ 0.2 km/s decrease in V_s at ~ 4 km depth, which may represent the lithological boundary between the BTG and the metasedimentary basement of the Sajahat Formation. Arrows depict the hydrothermal circulation system proposed for the SHS in North Singapore. Within this system, surface water from high elevations infiltrates a potential aquifer within the porous metasedimentary basement, heats up, and then rises due to buoyancy to the fractured geothermal reservoir in Yishun, ultimately supplying the SHS through faults and fractures. Note that the sketch is not to scale. SHS – Sembawang Hot Spring; SF – Seletar Fault.

Our study offers a seismic reference model for later geothermal investigations in Singapore. Based on the model, we tentatively recommend the Yishun District as the next exploratory deep drilling site, as the geothermal potential there is likely among the highest in the study area. On a broader scale, the geothermal process proposed for the SHS potentially provides new insight into the deep heat sources of numerous hot springs, and their associated geothermal resources, across the Southeast Asian batholiths. For example, similar to the SHS, most of the hot springs identified in West Malaysia occur within granitic rocks, close to faults and at the foothills of the western and central highlands (Fig. 1a). These findings underline the roles of high radioactive heat-producing rocks, structural weakness and relief contrasts in shaping geothermal potential of non-volcanic regions.

5. Conclusions and outlook

We assess the geothermal potential of Singapore through a nodal seismic experiment around the SHS. The resulting images show clear variations in seismic velocity and discontinuity structures beneath the area. RFs indicate a downward decrease in V_s at ~ 4 km depth, likely marking the boundary between the upper BTG and the lower, possibly fluid-saturated metasediments of the Sajahat Formation. This discontinuity appears weaker beneath Yishun in the southeastern study area, where the shallow crust exhibits lower V_s (< 3.2 km/s) and higher V_p/V_s (> 2.1) compared to the surrounding regions. These observations suggest the existence of a shallow-crustal geothermal reservoir below Yishun. We propose that gravity-driven surface water descends from higher elevations, heats up at depth, and then rises to the highly fractured shallow reservoir that supplies the SHS. Our study provides structural references for later geothermal investigations in Singapore.

The present study has certain limitations. For example, we focus on isotropic structures but ignore anisotropy, which is prevalent in geothermal systems (e.g., Granados-Chavarria et al., 2022). Former studies indicate that a 10–20 % radial anisotropy would lower the isotropic V_s in granite under normal upper-crustal pressures by 5–10 % (Ward et al., 2014). Anisotropy, possibly triggered by extensive fractures and fluid movements, may therefore partially account for the V_s reduction in the proposed geothermal reservoir. Furthermore, our seismic images have high resolution in the upper ~ 5 km of the crust, with deeper structures remaining less constrained. In the absence of Cenozoic volcanism (Zhao et al., 2002) and with a felsic crustal V_p/V_s of 1.72 in the study area (e.g., Fig. 8a), the prime heat source at the SHS is likely the radiogenic elements within the shallow crust. However, some argue that the concentration of isotopes may be too low to generate sufficient heat (e.g., Tjawi, 2013), raising the possibility that additional heat sources, such as via volcanic or uppermost mantle processes, may be essential to fully explain the observed geothermal activity. This will be the task of future lithospheric-scale imaging. Additionally, since our data are primarily sensitive to seismic velocity and cover only a localized area, a more comprehensive assessment of the geothermal potential in Singapore, particularly in determining the exact geometry and resource capacity of the identified shallow-depth reservoir, will require the integration of additional geophysical and geological data in future studies.

CRediT authorship contribution statement

Yiming Bai: Writing – original draft, Visualization, Investigation, Data curation. **Shijie Hao:** Writing – review & editing, Methodology, Investigation, Data curation. **Jinyun Xie:** Writing – review & editing, Methodology, Investigation. **Mijian Xu:** Writing – review & editing, Methodology, Data curation. **Xiao Xiao:** Writing – review & editing, Investigation. **Jing Chen:** Writing – review & editing, Methodology, Data curation. **Chun Fei Chey:** Writing – review & editing, Data curation. **Dongdong Wang:** Writing – review & editing, Data curation. **Ping Tong:** Writing – review & editing, Supervision, Funding acquisition, Data curation, Conceptualization.

Declaration of competing interest

The authors declare that they have no known competing financial interests or personal relationships that could have appeared to influence the work reported in this paper.

Acknowledgments

This study is funded by Ministry of Education, Singapore, under its MOE AcRF Tier-2 grant (MOE-T2EP20122-0008). We appreciate the helpful comments from Paolo Frattini (Editor) and two anonymous reviewers. Local government agencies, including National Parks Board, Public Utilities Board, Ministry of Education and Singapore Land Authority, are gratefully acknowledged for issuing temporary occupation licenses for the study (with special thanks to Esindah Ismail, Sebastian Ow, Darren Tan and Roslinda Mohd Idris). We thank the Centre for Geohazard Observation at Nanyang Technological University, Yukuan Chen, Hongyu Zeng, Tianjue Li, Shucheng Wu, Xiaole Zhou, Yanan Xie, Junyi Xia and Jiayuan Yao for assistance in array deployment and maintenance. We also thank the Data Management Center of the Incorporated Research Institutions for Seismology (IRIS-DMC) for servicing the open access data (<http://ds.iris.edu/mda/MS/> and <http://ds.iris.edu/mda/MY/>). The surface-wave dispersion, RF and P -coda ACF data from this study can be visited through Bai et al. (2024). We use Seispy for receiver function computation (Xu and He, 2022) and SeisGo for ambient noise data processing (Yang et al., 2023). The code for adjoint-state surface-wave tomography is from Xu et al. (2025). The code for joint inversion of surface-wave dispersion and RF is from Guo et al. (2016). Forward modeling of dispersion and RF is performed using the propagator-matrix method and the reflectivity method, respectively (Herrmann, 2013; Shibutani et al., 1996). The 2-D waveform modeling code is from Li et al. (2014). Most of the figures are generated by PyGMT (Uieda et al., 2021).

Appendix A. Supplementary data

Supplementary data to this article can be found online at <https://doi.org/10.1016/j.enggeo.2025.107968>.

Data availability

I have shared the link to my data at the Attach File step

References

- Alfaró, C., Wallace, M., 1994. Origin and classification of springs and historical review with current applications. *Environ. Geol.* 24 (2), 112–124. <https://doi.org/10.1007/BF00767884>.
- Amatyakul, P., Siripunvaraporn, W., Rung-Arunwan, T., Vachiratienchai, C., Pirarai, K., Prommakorn, N., 2023. A decade of successful magnetotelluric surveys for delineating shallow geothermal reservoirs beneath nonvolcanic hot springs in Thailand. *Geophysics* WB55–WB69. <https://doi.org/10.1190/geo2022-0486.1>.
- Axelsson, G., Gunnlaugsson, E., Jónasson, T., Olafsson, M., 2010. Low-temperature geothermal utilization in Iceland – decades of experience. *Geothermics* 39 (4), 329–338. <https://doi.org/10.1016/j.geothermics.2010.09.002>.
- Bai, Y., Yao, J., Wu, S., Wei, S., Wang, Y., Rondenay, S., et al., 2023. Rapid along-strike variations of shallow crustal structure in response to Indo-Burma subduction: Constraints from multi-type passive seismic data. *Earth Planet. Sci. Lett.* 610, 118105. <https://doi.org/10.1016/j.epsl.2023.118105>.
- Bai, Y., Hao, S., Xie, J., Tong, P., 2024. Upporting data for geothermal exploration in Singapore by Bai et al. [Data set]. Figshare. <https://doi.org/10.6084/m9.figshare.28069904>.
- Baioumy, H., Nawawi, M., Wagner, K., Arifin, M.H., 2015. Geochemistry and geothermometry of non-volcanic hot springs in West Malaysia. *J. Volcanol. Geotherm. Res.* 290, 12–22. <https://doi.org/10.1016/j.jvolgeores.2014.11.014>.
- Barbier, E., 2002. Geothermal energy technology and current status: an overview. *Renew. Sust. Energ. Rev.* 6 (1), 3–65. [https://doi.org/10.1016/S1364-0321\(02\)00002-3](https://doi.org/10.1016/S1364-0321(02)00002-3).
- Bensen, G.D., Ritzwoller, M.H., Barmin, M.P., Levshin, A.L., Lin, F., Moschetti, M.P., et al., 2007. Processing seismic ambient noise data to obtain reliable broad-band surface wave dispersion measurements. *Geophys. J. Int.* 169 (3), 1239–1260. <https://doi.org/10.1111/j.1365-246X.2007.03374.x>.
- Boggs Jr., S., 2009. *Petrology of Sedimentary Rocks*. Cambridge University Press.
- Brace, W.F., 1980. Permeability of crystalline and argillaceous rocks. *Int. J. Rock Mech. Min. Sci. Geomech. Abstr.* 17 (5), 241–251. [https://doi.org/10.1016/0148-9062\(80\)9087-4](https://doi.org/10.1016/0148-9062(80)9087-4).
- Brocher, T.M., 2005. Empirical Relations between Elastic Wavespeeds and Density in the Earth's Crust. *Bull. Seismol. Soc. Am.* 95 (6), 2081–2092. <https://doi.org/10.1785/0120050077>.
- Chen, L., Cheng, C., Wei, Z., 2009. Seismic evidence for significant lateral variations in lithospheric thickness beneath the central and western North China Craton. *Earth Planet. Sci. Lett.* 286 (1), 171–183. <https://doi.org/10.1016/j.epsl.2009.06.022>.
- Cheng, F., Xia, J., Ajo-Franklin, J.B., Behm, M., Zhou, C., Dai, T., et al., 2021. High-resolution ambient noise imaging of geothermal reservoir using 3C dense seismic nodal array and ultra-short observation. *J. Geophys. Res. Solid Earth* 126 (8), e2021JB021827. <https://doi.org/10.1029/2021JB021827>.
- Christensen, N.I., 1965. Compressional wave velocities in metamorphic rocks at pressures to 10 kilobars. *J. Geophys. Res.* (1896–1977) 70 (24), 6147–6164. <https://doi.org/10.1029/JZ0701024p06147>.
- Christensen, N.I., 1996. Poisson's ratio and crustal seismology. *J. Geophys. Res. Solid Earth* 101 (B2), 3139–3156. <https://doi.org/10.1029/95JB03446>.
- Christensen, N.I., Mooney, W.D., 1995. Seismic velocity structure and composition of the continental crust: a global view. *J. Geophys. Res. Solid Earth* 100 (B6), 9761–9788. <https://doi.org/10.1029/95JB00259>.
- Christensen, N.I., Salisbury, M.H., 1973. Velocities, elastic moduli and weathering-age relations for pacific layer 2 basaltas. *Earth Planet. Sci. Lett.* 19 (4), 461–470. [https://doi.org/10.1016/0012-821X\(73\)90190-8](https://doi.org/10.1016/0012-821X(73)90190-8).
- Curewitz, D., Karson, J.A., 1997. Structural settings of hydrothermal outflow: Fracture permeability maintained by fault propagation and interaction. *J. Volcanol. Geotherm. Res.* 79 (3), 149–168. [https://doi.org/10.1016/S0377-0273\(97\)00027-9](https://doi.org/10.1016/S0377-0273(97)00027-9).
- Delph, J.R., Levander, A., Niu, F., 2019. Constraining crustal properties using receiver functions and the autocorrelation of earthquake-generated body waves. *J. Geophys. Res. Solid Earth* 124 (8), 8981–8997. <https://doi.org/10.1029/2019JB017929>.
- Dodd, T.J.H., Gillespie, M.R., Leslie, A.G., Kearsey, T.I., Kendall, R.S., Bide, T.P., et al., 2019. Paleozoic to Cenozoic sedimentary bedrock geology and lithostratigraphy of Singapore. *J. Asian Earth Sci.* 180, 103878. <https://doi.org/10.1016/j.jseas.2019.103878>.
- Domra Kana, J., Djongyang, N., Raidandi, Danwe, Njandjock Nouck, P., Dadjé, Abdouramani, 2015. A review of geophysical methods for geothermal exploration. *Renew. Sust. Energ. Rev.* 44, 87–95. <https://doi.org/10.1016/j.rser.2014.12.026>.
- Eberhart-Phillips, D., Han, D.-H., Zoback, M.D., 1989. Empirical relationships among seismic velocity, effective pressure, porosity, and clay content in sandstone. *Geophysics* 54 (1), 82–89. <https://doi.org/10.1190/1.1442580>.
- Efron, B., 1992. Bootstrap methods: another look at the Jackknife. In: Kotz, S., Johnson, N.L. (Eds.), *Breakthroughs in Statistics: Methodology and Distribution*. Springer, New York, NY, pp. 569–593. https://doi.org/10.1007/978-1-4612-4380-9_41.
- Fliedner, M.M., Klemperer, S.L., Christensen, N.I., 2000. Three-dimensional seismic model of the Sierra Nevada arc, California, and its implications for crustal and upper mantle composition. *J. Geophys. Res. Solid Earth* 105 (B5), 10899–10921. <https://doi.org/10.1029/2000JB900029>.
- Gillespie, M.R., Kendall, R.S., Leslie, A.G., Millar, I.L., Dodd, T.J.H., Kearsey, T.I., et al., 2019. The igneous rocks of Singapore: New insights to Palaeozoic and Mesozoic assembly of the Sukhothai Arc. *J. Asian Earth Sci.* 183, 103940. <https://doi.org/10.1016/j.jseas.2019.103940>.
- Granados-Chavarría, I., Calò, M., Figueroa-Soto, Á., Jousset, P., 2022. Seismic imaging of the magmatic plumbing system and geothermal reservoir of the Los Humeros caldera (Mexico) using anisotropic shear wave models. *J. Volcanol. Geotherm. Res.* 421, 107441. <https://doi.org/10.1016/j.jvolgeores.2021.107441>.
- Guo, Z., Chen, Y.J., Ning, J., Yang, Y., Afonso, J.C., Tang, Y., 2016. Seismic evidence of on-going sublithosphere upper mantle convection for intra-plate volcanism in Northeast China. *Earth Planet. Sci. Lett.* 433, 31–43. <https://doi.org/10.1016/j.epsl.2015.09.035>.
- Hall, R., Morley, C.K., 2004. Sundaland Basins. In: *Continent-Ocean Interactions within East Asian Marginal Seas*. American Geophysical Union (AGU), pp. 55–85. <https://doi.org/10.1029/149GM04>.
- Hao, S., Chen, J., Xu, M., Tong, P., 2024. Topography-Incorporated Adjoint-State Surface Wave Traveltime Tomography: Method and a Case Study in Hawaii. *J. Geophys. Res. Solid Earth* 129 (1), e2023JB027454. <https://doi.org/10.1029/2023JB027454>.
- Herrmann, R.B., 2013. Computer programs in seismology: an evolving tool for instruction and research. *Seismol. Res. Lett.* 84 (6), 1081–1088. <https://doi.org/10.1785/0220110096>.
- Hirt, C., Claessens, S., Fecher, T., Kuhn, M., Pail, R., Rexer, M., 2013. New ultrahigh-resolution picture of Earth's gravity field. *Geophys. Res. Lett.* 40 (16), 4279–4283. <https://doi.org/10.1002/grl.50838>.
- Hutchison, C.S., Tan, D.N.K., 2009. *Geology of Peninsular Malaysia. Published jointly by the University of Malaya [and] the Geological Society of Malaysia*.
- Julian, B.R., Ross, A., Foulger, G.R., Evans, J.R., 1996. Three-dimensional seismic image of a geothermal reservoir: the Geysers, California. *Geophys. Res. Lett.* 23 (6), 685–688. <https://doi.org/10.1029/95GL0321>.
- Kennett, B.L.N., Engdahl, E.R., 1991. Traveltimes for global earthquake location and phase identification. *Geophys. J. Int.* 105 (2), 429–465. <https://doi.org/10.1111/j.1365-246X.1991.tb06724.x>.
- Kern, H., Richter, A., 1981. Temperature derivatives of compressional and shear wave velocities in crustal and mantle rocks at 6 kbar confining pressure. *J. Geophys.* 49 (1), 47–56.

- Kind, R., Yuan, X., Saul, J., Nelson, D., Sobolev, S.V., Mechie, J., et al., 2002. Seismic images of crust and upper mantle beneath Tibet: evidence for Eurasian Plate subduction. *Science* 298 (5596), 1219–1221. <https://doi.org/10.1126/science.1078115>.
- Kolzenburg, S., Heap, M.J., Lavallée, Y., Russell, J.K., Meredith, P.G., Dingwell, D.B., 2012. Strength and permeability recovery of tuffsite-bearing andesite. *Solid Earth* 3 (2), 191–198. <https://doi.org/10.5194/se-3-191-2012>.
- Lee, K.W., Zhou, Y., 2009. *Geology of Singapore*, 2nd ed. Defence Science and Technology Agency, Singapore.
- Leslie, A.G., Dodd, T.J.H., Gillespie, M.R., Kendall, R.S., Bide, T.P., Kearsey, T.I., et al., 2019. Ductile and brittle deformation in Singapore: a record of Mesozoic orogeny and amalgamation in Sundaland, and of post-orogenic faulting. *J. Asian Earth Sci.* 181, 103890. <https://doi.org/10.1016/j.jseaes.2019.103890>.
- Li, D., Helmberger, D., Clayton, R.W., Sun, D., 2014. Global synthetic seismograms using a 2-D finite-difference method. *Geophys. J. Int.* 197 (2), 1166–1183. <https://doi.org/10.1093/gji/ggu050>.
- Liberty, L., 1998. Seismic reflection imaging of a geothermal aquifer in an urban setting. *Geophysics* 63 (4), 1285–1294. <https://doi.org/10.1190/1.1444430>.
- Ligorría, J.P., Ammon, C.J., 1999. Iterative deconvolution and receiver-function estimation. *Bull. Seismol. Soc. Am.* 89 (5), 1395–1400. <https://doi.org/10.1785/BSSA0890051395>.
- Lin, F.-C., Li, D., Clayton, R.W., Hollis, D., 2013. High-resolution 3D shallow crustal structure in Long Beach, California: Application of ambient noise tomography on a dense seismic array. *Geophysics* 78 (4), Q45–Q56. <https://doi.org/10.1190/geo2012-0453.1>.
- Liu, X., Hu, K., Qian, R., Zhao, S., Zhang, J., Ling, J., et al., 2025. 3D high-density ambient noise imaging of the Nankou-Sunhe buried active fault in Beijing. *Eng. Geol.* 345, 107862. <https://doi.org/10.1016/j.engegeo.2024.107862>.
- Luo, Y., Yang, Y., Xu, Y., Xu, H., Zhao, K., Wang, K., 2015. On the limitations of interstation distances in ambient noise tomography. *Geophys. J. Int.* 201 (2), 652–661. <https://doi.org/10.1093/gji/ggv043>.
- Lythgoe, K., Ong Su Qing, M., Wei, S., 2020. Large-scale crustal structure beneath Singapore using receiver functions from a dense urban nodal array. *Geophys. Res. Lett.* 47 (7), e2020GL087233. <https://doi.org/10.1029/2020GL087233>.
- Macpherson, K.A., Hidayat, D., Feng, L., Goh, S.H., 2013. Crustal thickness and velocity structure beneath Singapore's seismic network. *J. Asian Earth Sci.* 64, 245–255. <https://doi.org/10.1016/j.jseaes.2012.12.027>.
- Mavko, G., Mukerji, T., Dvorkin, J., 2020. *The Rock Physics Handbook*, 3rd ed. Cambridge University Press, Cambridge. <https://doi.org/10.1017/9781108333016>.
- Metcalfe, I., 2000. The Bentong–Raub Suture Zone. *J. Asian Earth Sci.* 18 (6), 691–712. [https://doi.org/10.1016/S1367-9120\(00\)00043-2](https://doi.org/10.1016/S1367-9120(00)00043-2).
- Metcalfe, I., 2013. Tectonic evolution of the Malay Peninsula. *J. Asian Earth Sci.* 76, 195–213. <https://doi.org/10.1016/j.jseaes.2012.12.011>.
- Mosegaard, K., Tarantola, A., 1995. Monte Carlo sampling of solutions to inverse problems. *J. Geophys. Res. Solid Earth* 100 (B7), 12431–12447. <https://doi.org/10.1029/94JB03097>.
- Muksin, U., Haberland, C., Bauer, K., Weber, M., 2013. Three-dimensional upper crustal structure of the geothermal system in Tarutung (North Sumatra, Indonesia) revealed by seismic attenuation tomography. *Geophys. J. Int.* 195 (3), 2037–2049. <https://doi.org/10.1093/gji/ggt383>.
- Muñoz, G., 2014. Exploring for geothermal resources with electromagnetic methods. *Surv. Geophys.* 35 (1), 101–122. <https://doi.org/10.1007/s10712-013-9236-0>.
- Ng, S.W.-P., Whitehouse, M.J., Searle, M.P., Robb, L.J., Ghani, A.A., Chung, S.-L., et al., 2015. Petrogenesis of Malaysian granitoids in the Southeast Asian tin belt: part 2. U-Pb zircon geochronology and tectonic model. *GSA Bull.* 127 (9–10), 1238–1258. <https://doi.org/10.1130/B31214.1>.
- Nilot, E., Li, Y.E., Lythgoe, K., 2020. Bedrock detection based on seismic interferometry using ambient noise in Singapore. In: SEG Technical Program Expanded Abstracts 2020. Society of Exploration Geophysicists, pp. 3577–3581. <https://doi.org/10.1190/segam2020-3427558.1>.
- O'Connell, R.J., Budiansky, B., 1974. Seismic velocities in dry and saturated cracked solids. *J. Geophys. Res.* (1896–1977) 79 (35), 5412–5426. <https://doi.org/10.1029/JB079i035p05412>.
- Oliver, G., Palmer, A.C., Tjiawi, H., Zulkifli, F., 2011. Engineered geothermal power systems for Singapore. *IES J. Part A* 4 (4), 245–253. <https://doi.org/10.1080/19373260.2011.598261>.
- Oliver, G., Zaw, K., Hotson, M., Meffre, S., Manka, T., 2014. U-Pb zircon geochronology of Early Permian to Late Triassic rocks from Singapore and Johor: A plate tectonic reinterpretation. *Gondwana Res.* 26 (1), 132–143. <https://doi.org/10.1016/j.gr.2013.03.019>.
- Pan, X., Guo, W., Aung, Z., Nyo, A.K., Chiam, K., Wu, D., Chu, J., 2018. Procedure for establishing a 3D geological model for Singapore. In: Shi, X., Liu, Z., Liu, J. (Eds.), *Proceedings of GeoShanghai 2018 International Conference: Transportation Geotechnics and Pavement Engineering*. Springer, Singapore, pp. 81–89. https://doi.org/10.1007/978-981-13-0011-0_9.
- Paquet, J., Francois, P., Nedelec, A., 1981. Effect of partial melting on rock deformation: Experimental and natural evidences on rocks of granitic compositions. *Tectonophysics* 78 (1), 545–565. [https://doi.org/10.1016/0040-1951\(81\)90028-7](https://doi.org/10.1016/0040-1951(81)90028-7).
- Park, J., Levin, V., 2002. Seismic anisotropy: tracing plate dynamics in the mantle. *Science* 296 (5567), 485–489. <https://doi.org/10.1126/science.1067319>.
- Petford, N., Cruden, A.R., McCaffrey, K.J.W., Vigneresse, J.-L., 2000. Granite magma formation, transport and emplacement in the Earth's crust. *Nature* 408 (6813), 669–673. <https://doi.org/10.1038/35047000>.
- Pham, T.-S., Tkalcic, H., 2017. On the feasibility and use of teleseismic P wave coda autocorrelation for mapping shallow seismic discontinuities. *J. Geophys. Res. Solid Earth* 122 (5), 3776–3791. <https://doi.org/10.1002/2017JB013975>.
- Planès, T., Obermann, A., Antunes, V., Lupi, M., 2020. Ambient-noise tomography of the Greater Geneva Basin in a geothermal exploration context. *Geophys. J. Int.* 220 (1), 370–383. <https://doi.org/10.1093/gji/ggz457>.
- Qin, T., Lu, L., Ding, Z., Feng, X., Zhang, Y., 2022. High-resolution 3D shallow S wave velocity structure of Tongzhou, subcenter of Beijing, inferred from multimode Rayleigh Waves by beamforming seismic noise at a dense array. *J. Geophys. Res. Solid Earth* 127 (5), e2021JB023689. <https://doi.org/10.1029/2021JB023689>.
- Shibutani, T., Sambridge, M., Kennett, B., 1996. Genetic algorithm inversion for receiver functions with application to crust and uppermost mantle structure beneath eastern Australia. *Geophys. Res. Lett.* 23 (14), 1829–1832. <https://doi.org/10.1029/96GL01671>.
- Spencer Jr., J.W., Nur, A.M., 1976. The effects of pressure, temperature, and pore water on velocities in westerly granite. *J. Geophys. Res.* (1896–1977) 81 (5), 899–904. <https://doi.org/10.1029/JB081i005p00899>.
- Stober, I., Bucher, K., 2021. *Geothermal Energy: From Theoretical Models to Exploration and Development*. Springer International Publishing, Cham. <https://doi.org/10.1007/978-3-030-71685-1>.
- Tan, C., 2024, April 18. Two-year study to determine S'pore's geothermal potential to start later in 2024. The Straits Times. Retrieved from. <https://str.sg/FK6R>.
- Tjiawi, H., 2013, September 5. Numerical Simulation Studies of the Geothermal Resource in Singapore (Thesis). Retrieved from. <https://scholarbank.nus.edu.sg/handle/10635/80059>.
- Toksöz, M.N., Cheng, C.H., Timur, A., 1976. Velocities of seismic waves in porous rocks. *Geophysics* 41 (4), 621–645. <https://doi.org/10.1190/1.1440639>.
- Tong, P., 2021. Adjoint-state traveltime tomography: eikonal equation-based methods and application to the Anza Area in Southern California. *J. Geophys. Res. Solid Earth* 126 (5), e2021JB021818. <https://doi.org/10.1029/2021JB021818>.
- Uieda, L., Tian, D., Leong, W.J., Toney, L., Schlitzer, W., Grund, M., et al., 2021. PyGMT: A Python Interface for the Generic Mapping Tools. <https://doi.org/10.5281/ZENODO.4522136>.
- Védrine, S., Bretaudeau, F., Darnet, M., Hautot, S., Tarits, P., 2023. Exploring geothermal resources using electromagnetic methods in coastal areas of volcanic islands: challenges of nearshore and land 3D controlled-source electromagnetic data. *Geophysics* WB133–WB149. <https://doi.org/10.1190/geo2022-0482.1>.
- Ward, K.M., Zandt, G., Beck, S.L., Christensen, D.H., McParlin, H., 2014. Seismic imaging of the magmatic underpinnings beneath the Altiplano-Puna volcanic complex from the joint inversion of surface wave dispersion and receiver functions. *Earth Planet. Sci. Lett.* 404, 43–53. <https://doi.org/10.1016/j.epsl.2014.07.022>.
- Xiao, X., Cheng, S., Wu, J., Wang, W., Sun, L., Wang, X., Wen, L., 2021. Shallow seismic structure beneath the continental China revealed by P-wave polarization, Rayleigh wave ellipticity and receiver function. *Geophys. J. Int.* 225 (2), 998–1019. <https://doi.org/10.1093/gji/ggab022>.
- Xu, M., He, J., 2022. Seispy: python module for batch calculation and postprocessing of receiver functions. *Seismol. Res. Lett.* 94 (2A), 935–943. <https://doi.org/10.1785/0220220288>.
- Xu, M., Hao, S., Chen, J., Zhang, B., Tong, P., 2025. SurfATT: high-performance package for adjoint-state surface-wave travel-time tomography. *Seismol. Res. Lett.* <https://doi.org/10.1785/0220240206>.
- Yang, X., Bryan, J., Okubo, K., Jiang, C., Clements, T., Denolle, M.A., 2023. Optimal stacking of noise cross-correlation functions. *Geophys. J. Int.* 232 (3), 1600–1618. <https://doi.org/10.1093/gji/ggac410>.
- Yao, H., van Der Hilst, R.D., de Hoop, M.V., 2006. Surface-wave array tomography in SE Tibet from ambient seismic noise and two-station analysis — I. Phase velocity maps. *Geophys. J. Int.* 166 (2), 732–744. <https://doi.org/10.1111/j.1365-246X.2006.03028.x>.
- Zhao, J., 1998. Rock mass hydraulic conductivity of the Bukit Timah granite, Singapore. *Eng. Geol.* 50 (1), 211–216. [https://doi.org/10.1016/S0013-7952\(98\)00021-0](https://doi.org/10.1016/S0013-7952(98)00021-0).
- Zhao, J., Chen, C.N., Cai, J.G., 2002. A hydrogeological study of the Sembawang hot spring in Singapore. *Bull. Eng. Geol. Environ.* 61 (1), 59–71. <https://doi.org/10.1007/s10064-001-0143-0>.
- Zhu, L., Kanamori, H., 2000. Moho depth variation in southern California from teleseismic receiver functions. *J. Geophys. Res. Solid Earth* 105 (B2), 2969–2980. <https://doi.org/10.1029/1999JB900322>.